

# THE EJECTION VELOCITIES OF INTERSTELLAR OBJECTS SIGNPOST THEIR PROGENITOR SYSTEM ARCHITECTURES

LEAH ALBROW <sup>1,2</sup>, MICHELE T. BANNISTER <sup>1</sup>, JOHN C. FORBES <sup>1</sup>, DAVID NESVORNÝ <sup>3</sup>

<sup>1</sup>School of Physical and Chemical Sciences—Te Kura Matū, University of Canterbury, Christchurch 8140, New Zealand

<sup>2</sup>Department of Earth, Atmospheric, and Planetary Sciences, Massachusetts Institute of Technology, 77 Massachusetts Avenue, Cambridge, MA 02139, USA

<sup>3</sup>Department of Space Studies, Southwest Research Institute, 1301 Walnut St., Suite 400, Boulder, CO 80302, USA

Version December 5, 2025

## ABSTRACT

Interstellar objects (ISOs) ejected from planetary systems carry kinematic signatures of their formation environments. The properties of these velocity distributions govern the ISOs’ propagation and dynamical evolution in the Galactic potential. We investigate how planetary system architecture influences ISO production during post-gas-disc dynamical instabilities using N-body simulations. We explore the ISO production outcomes of 2461 randomly-generated systems, spanning system masses of 300–800  $M_{\oplus}$  and multiplicities of 3–7 planets. Integrating planets in a disc of test particles for 10 Myr, we find that the evolving systems can be broadly divided into two distinct classes based on their initial architectures. *Catastrophic systems* are characterised by high-multiplicity and orbitally-compact architectures, or by having high-mass planets in systems with large mass asymmetries. These systems eject a high fraction of planetesimals (median 59%) and, depending on the ejection pathway, eject ISOs at high speeds (median  $2.9 \text{ km s}^{-1}$ ). Alternatively, *quiet systems* have lower masses and multiplicities, and do not undergo significant orbital changes, but are still able to eject a median of 28% of planetesimals at low velocities (median  $1.6 \text{ km s}^{-1}$ ). This points to different ejection pathways, involving either violent global instabilities or more gradual, diffusive processes. We find the ejection velocities of ISOs are typically low, on the order of a few  $\text{km s}^{-1}$ . Although ISOs will then experience dynamical heating as they orbit the Galaxy, their velocity distributions retain signatures of their progenitor systems’ architectures and histories, pointing to the future use of ISOs in Galactic archaeology.

*Subject headings:* Interstellar objects (52), Exoplanet dynamics (490), Interdisciplinary astronomy (804)

## 1. INTRODUCTION

Interstellar objects (ISOs) are formed in protoplanetary discs and are subsequently unbound from their host star through a variety of proposed dynamical processes (e.g. The ‘Oumuamua ISSI Team et al. 2019). Once unbound, they traverse the Galaxy, with their long-term evolution driven by their initial ejection velocities. As ISOs orbit within the Galactic potential, differences in ejection velocities stretch unbound populations into tidal streams. Forbes et al. (2025) demonstrated that stream properties—size, density structure, and kinematics—are shaped primarily by the initial velocity dispersion, with secondary contributions from Galactic perturbations. This dispersion is set by the initial spread in ejection velocities. Subsequent dynamical heating occurs from non-axisymmetric perturbations in the Galactic potential. Understanding how ISOs are ejected and their associated velocities is therefore crucial for studying their distribution throughout the Galaxy.

ISOs must first be produced before their Galactic dynamics matter. Planetesimal formation appears ubiquitous in young protoplanetary discs, the mechanisms for which are outlined in a recent review by Drazkowska et al. (2023). The frequency at which planetesimals and dust grains are ejected during the gas-disc phase remains unconstrained. Eriksson et al. (2021) find that, in planetesimal disc simulations which include effects such as gas drag and mass ablation to simulate the presence of the gas disc, 15–40% of planetesimals formed at the edges of planetary gaps are ejected. Further work is needed to understand how gas drag and disc turbulence affect planetesimal ejection rates during this phase.

In this work we focus on systems after gas disc dispersal, by processes such as magnetic winds, turbulence, stellar encounters, or external photo-evaporation (Hasegawa et al. 2022; Alexander et al. 2014), leaving a population of giant planets, and planetesimals. After disc dispersal, gravitational scattering between planetesimals and the system’s massive planets becomes a dominant dynamical process. Gravitational scattering can drive planetary migration (Levison et al. 2007), and in the case of inward migration, scatters planetesimals onto larger orbits. In the Solar System, gas dispersal has been linked to the onset of a large-scale dynamical instability (Liu et al. 2022). Because most modelling efforts focus on retained populations, either to reproduce observed exoplanet architectures or to match the precisely measured small-body populations of the Solar System (e.g. Bannister et al. 2018; Pfalzner et al. 2024), ejected material has received far less attention. For example, in a typical Solar System simulation from Nesvorný et al. (2023), 93.4% of planetesimals initially placed between 4 and 30 au were ejected over the 4.5 Gyr of the simulation. Given the broad diversity of exoplanetary systems, whether this high ejection fraction is typical remains unclear, though this has long

\*E-mail: lalbrow@mit.edu

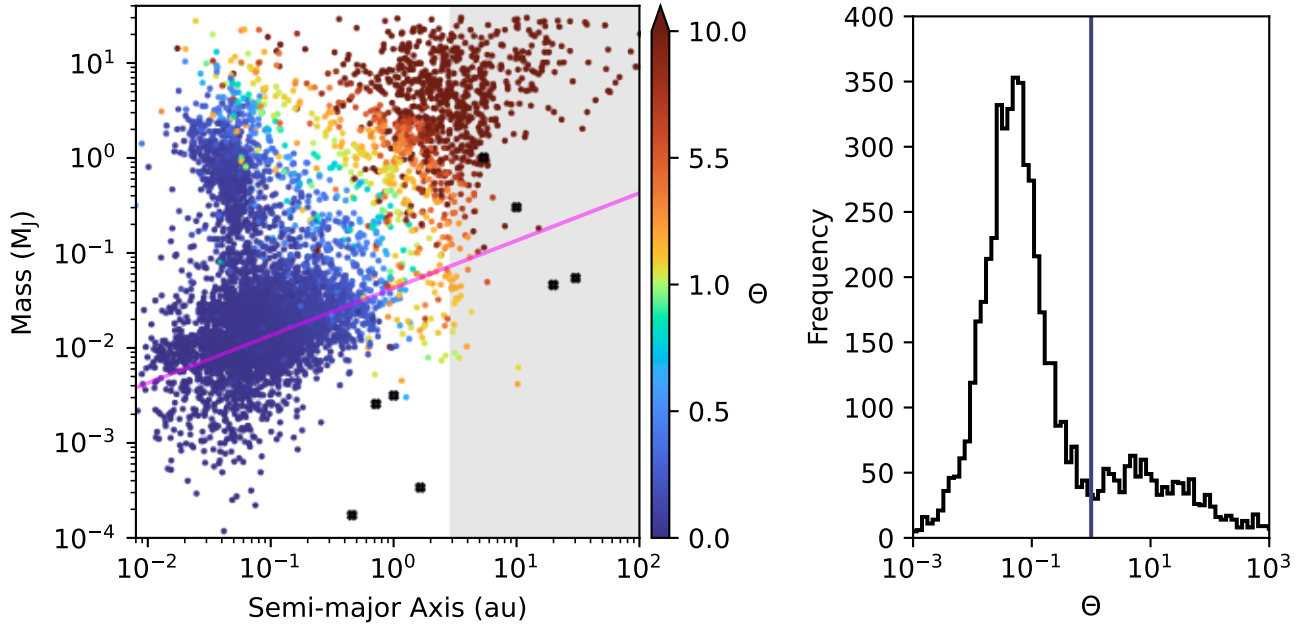


FIG. 1.— **Left:** Safronov number for the population of known exoplanets, following Fig. 1 of Laughlin & Batygin (2017). Only planets with measured masses and radii are shown (data from the NASA Exoplanet Archive, 22 Nov 2025). Solar System planets are plotted as larger symbols with black outlines. The pink line indicates a radial-velocity semi-amplitude precision of 1 m s<sup>-1</sup> (Lovis & Fischer 2010), indicating the approximate detection threshold for RV surveys. The grey shaded region marks the Kepler primary mission duration, serving as a proxy for transit-survey sensitivity. **Right:** distribution of  $\Theta$  for the exoplanets in the left panel. Most known exoplanets have  $\Theta \ll 1$ , implying that their dynamical interactions are collision-dominated rather than ejection-dominated.

been used as a suitable initial assumption (e.g. Stern 1990; Moro-Martín et al. 2009; Raymond et al. 2020; Lintott et al. 2021).

Beyond instability-driven ejections, several other mechanisms may contribute to the ISO population. Since most ISOs are thought to be ejected by early-system processes, the birth cluster environment likely plays a significant role in their dynamical evolution. Stellar flybys, common in dense stellar environments (Malmberg et al. 2011), can perturb outer disc populations and eject ISOs with typical velocities between 0.5 and 2 km s<sup>-1</sup> relative to the host star (Pfalzner et al. 2021). Such encounters may also trigger planetary instabilities that further enhance ISO production.

Finally, evolved stars are hypothesised to produce ISOs. A small wave of ISOs may be gently unbound during the asymptotic giant branch (AGB) phase of stellar evolution (e.g. Veras et al. 2014; Levine et al. 2023). According to ejection velocities reported in Pfalzner et al. (2021) (based on unpublished work from Veras et al. (2014)), these objects have mean ejection velocities below 0.5 km s<sup>-1</sup>.

Dynamical instabilities are an underexplored yet significant mechanism for releasing large fractions of a system’s planetesimals as ISOs. Morbidelli (2018) outlined several potential triggers for global instabilities, including destabilization following disc dispersal, the formation of planets in close proximity (within a few Hill radii), capture into orbital resonances, secular chaotic evolution, tidal interactions with the host star, and external perturbations. Such instabilities appear to be common. For example, Izidoro et al. (2017) found that, to reproduce the observed Kepler sample, more than 75% of multi-planet systems hosting super-Earths must have undergone a dynamical instability after gas dispersal. Additional observational evidence comes from the discovery of high-eccentricity hot Jupiters, whose in-situ formation is considered unlikely (Dawson & Johnson 2018). Significant dynamical evolution thus likely produced these planets, requiring either a distant perturber or planetary companion.

The impact of dynamical instabilities on planetesimal fates is the central focus of this work. A key quantity governing these outcomes is the Safronov number,

$$\Theta = \frac{v_{\text{esc}}^2}{v_c^2} = \frac{2M_p a_p}{M_* R_p}, \quad (1)$$

which characterizes the ratio of ejections to planet–planetesimal collisions (Safronov 1972). Here  $v_{\text{esc}}$  is the planet’s escape speed and  $v_c$  is its circular orbital velocity around a star of mass  $M_*$ . A planet with  $\Theta \gtrsim 1$  typically ejects planetesimals during close encounters rather than accreting them. In the case where the Safronov number is less than one, collisions are more likely. Laughlin & Batygin (2017) argue that the existence of ISOs requires a population of exoplanets capable of efficiently ejecting material, that is, planets with a Safronov number greater than or equal to one. As illustrated in Figure 1, the currently known exoplanet sample is strongly biased: short-period, large-radius planets are overrepresented, while long-period intermediate-mass planets remain under-detected. A substantial population of efficient planetesimal ejectors may lie in the bottom-right regions of the left panel, where current detection methods are incomplete. The right panel of Figure 1 shows the majority of known exoplanets cannot efficiently eject

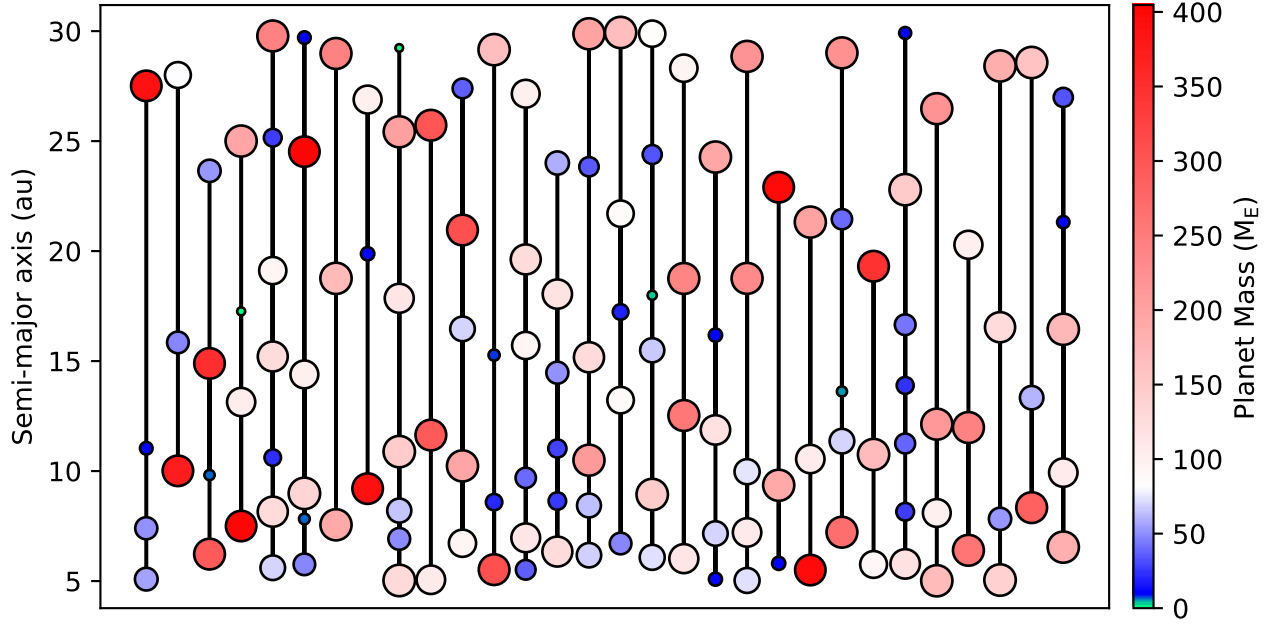


FIG. 2.— Thirty of the generated initial system configurations. Colour encodes planetary mass, indicating approximate compositional categories. Red planets are larger than  $80 M_{\oplus}$  (gas giants), and blue planets are from  $5\text{--}80 M_{\oplus}$  (gas and ice giants). The green planets are below  $5 M_{\oplus}$ , indicating terrestrial planets. Symbol sizes are proportional to planetary radii calculated from Equation 2.

ISOs. Because our interest lies in ISO ejection, we focus on systems dominated by planets with Safronov numbers greatly exceeding unity. Rather than attempting to correct for exoplanet observational biases, we instead investigate ensembles of randomly generated planetary system architectures (see e.g., [Gautham Bhaskar & Perets 2025](#), for a similar approach), with an emphasis on the outer planets.

We begin by describing our N-body simulations ([section 2](#)), then examine the dynamical evolution of a representative system to illustrate key ejection mechanisms ([subsection 3.1](#)). Statistical analysis of our full simulation ensemble ([subsection 3.2](#)) reveals different pathways to ejection based on planetary system architectures, and trends in the inclinations of ejected ISOs, which are directly relevant for modelling ISO tidal streams ([Forbes et al. 2025](#)). We then use clustering methods ([subsection 3.3](#)) to find trends in the system architectures of systems with similar ejection velocity distributions. Finally, in [section 4](#) we consider the broader implications of our findings and outline directions for future work.

## 2. PLANETARY SYSTEM INTEGRATIONS

### 2.1. Dynamical Instability Simulations

We simulated the evolution of planetary systems embedded within discs of massless particles, exploring a wide range of system architectures. These simulations were conducted using the `rebound` Python package ([Rein & Liu 2012](#)). We used the `MERCURIUS` hybrid integrator, which employs a symplectic Wisdom-Holman integrator (`WHFast`) for well-separated particles and switches to a high-order integrator (`IAS15`) during close encounters ([Wisdom & Holman 1991](#); [Rein & Tamayo 2015](#); [Rein et al. 2019](#)). The threshold for switching to close-encounter mode was set at three Hill radii from the planets.

We focused on ISO production during dynamical instabilities rather than long-term stability, so we integrated systems for 10 Myr. Given the high masses of the simulated systems, which drive stronger gravitational perturbations and shorter dynamical timescales, this duration was sufficient for numerous instabilities to develop. Simulation states were stored in the `Simulationarchive` format ([Rein & Tamayo 2017](#)), allowing efficient storage and processing of particle trajectories.

A total of 2,500 planetary systems were generated as follows. The total mass of planets in the systems took values of 300, 400, 500, 600, 700, and  $800 M_{\oplus}$  (for comparison, the Solar System’s planetary mass is  $\sim 335 M_{\oplus}$ ). The initial multiplicity (number of planets) ranged from 3 to 7. 100 systems were created for each combination of multiplicity and total system mass. Several simulations did not finish running due to computational limitations, leaving a total of 2461 completed simulations. Individual planet masses were drawn from a symmetric Dirichlet distribution, which produces  $n$  positive values (where  $n$  is the system multiplicity) summing to unity. We used a concentration parameter of  $\alpha = 1$ , corresponding to a uniform distribution over all possible mass partitions. We then scaled these fractions by the system’s total planetary mass to obtain individual planet masses. The star was fixed at one solar mass.

For each system, planetary semi-major axes were randomly drawn, with equal probability, from 10,000 candidate positions uniformly distributed between 5 and 30 au. Planets were assigned to positions randomly without regard to mass. We then masked regions within eight Hill radii of each placed planet to prevent overlaps. In cases where no valid placements remained – particularly in higher-mass systems – the exclusion radius was gradually reduced until

all planets could be placed. For the highest mass systems, the minimum number of Hill radii was decreased to 5.2. Examples of the generated planetary systems are shown in [Figure 2](#). Planetesimals were placed in a similar fashion, but with a reduced minimum of four Hill radii separation from the planets. This sampling scheme yields, on average, both a planet and a planetesimal surface density profile  $\propto r^{-1}$ , though with considerable system-to-system scatter for the planets.

No additional stability constraints were imposed during system generation. Instead, systems were allowed to evolve naturally and were expected to undergo dynamical instability over the 10 Myr integration due to their high mass and compactness. Planets were treated as point masses during the integrations, but were later assigned estimated radii using the mass–radius relationship from [Müller et al. \(2024\)](#):

$$R = \begin{cases} 1.02 M^{0.27} & \text{if } M < 4.37, \\ 0.56 M^{0.67} & \text{if } 4.37 \leq M < 127, \\ 18.6 M^{-0.06} & \text{if } M \geq 127, \end{cases} \quad (2)$$

where  $M$  and  $R$  are in Earth units. This estimated radius is needed to calculate some of the system architecture parameters later introduced in [Table 1](#).

Each system had 10,000 massless planetesimals as a proxy for a mildly heated debris disc, extending from 5 to 40 au from the central star as described above. Orbital parameters for both planets and planetesimals were initialized from the following distributions: eccentricities drawn uniformly with  $0 \leq e \leq 0.1$ , inclinations between  $0 \leq i \leq 0.1$  radians, and true anomaly ( $f$ ), argument of periapsis ( $\omega$ ), and longitude of ascending node ( $\Omega$ ) drawn uniformly between 0 and  $2\pi$ . These ranges were chosen to represent a warm, but not yet dynamically excited, disc. Because the planetesimals were massless and thus could not self-excite, slightly more dynamically excited initial conditions were adopted to approximate natural disc heating. All planetesimals were treated as point particles in the integrations.

Planets were removed from the simulation if they satisfied either of the following conditions: (1)  $e > 1$  and  $r > 200$  au or (2)  $a > 1000$  au and  $e > 0.95$ . The radial distance threshold prevents premature removal of planets still interacting with the planetesimal disc. To ensure complete tracking of all ejection events, test particles were never removed. At the end of the simulation, ISOs were identified as all test particles with  $e > 1$ . We calculated their barycentric ejection velocities ( $v_\infty$ ) for analysis.

Because planets were treated as point masses<sup>1</sup>, they may yield unrealistically large ejection velocities. In reality, planetesimals approaching too closely would either collide with the planetary surface or undergo tidal disruption, depending on their internal strength. To account for physical collisions, we applied an upper velocity cutoff as follows: the maximum possible heliocentric  $v_\infty$  following an encounter with a planet is  $2\sqrt{1 + \sqrt{2}} \approx 3.1$  times the planet’s circular velocity, assuming the planet is on a nearly circular orbit. This limit corresponds to the case where a planetesimal can approach arbitrarily close to a point-mass planet ( $\Theta \rightarrow \infty$ ). In the opposite limit where  $\Theta \rightarrow 0$ , the maximum possible  $v_\infty$  approaches zero. For Safronov numbers of order 10–100, we find numerically that the maximum  $v_\infty/v_c \approx 2$ . We therefore filter out  $v_\infty$  values above

$$v_{\max} = 2 \max(v_p), \quad (3)$$

where  $\max(v_p)$  is the circular velocity of the innermost planet in the system. Since our initial minimum semi-major axis is 5 au, this imposes a maximum velocity of  $\sim 27$  km s<sup>−1</sup>. We checked our systems for inward migration of the planets, and adjusted this limit if any planets had final  $a < 5$  au. This filter excludes particles that would have collided with the planet’s physical surface in a more realistic simulation.

## 2.2. Solar System Simulation

We compared our results to a high-resolution Solar System evolution simulation by [Nesvorný et al. \(2023\)](#) (hereafter [N23](#)). This simulation included additional physical processes: planetary migration, instability, stellar encounters, and Galactic tides. The Solar System’s birth cluster was not a part of this simulation. The [N23](#) simulation spans 4.5 Gyr and defines ejected particles as those reaching a barycentric distance of 500,000 au. The initial population consisted of  $10^6$  particles distributed between 4 and 30 au, with a surface density scaling  $\propto r^{-1}$ . Bound particles which remained in the Oort Cloud were excluded from our analysis.

The positions and velocities of the particles reaching 500,000 au were recorded, along with the epoch at which they crossed this radius. To allow comparison with our `rebound` simulations, where particles are flagged as “ejected” at the time they are unbound, we calculated the time of ejection for the [N23](#) particles. For a hyperbolic orbit, the mean anomaly  $M$  is given by

$$M = \sqrt{\frac{\mu}{-a^3}}(t - \tau), \quad (4)$$

where  $\mu$  is the gravitational parameter ( $GM_*$ ),  $t$  is the time at which the particle reaches 500,000 au, and  $\tau$  is the time of the last perihelion passage. The orbital elements were computed from each particle’s position and velocity. From these, we extracted  $\tau$  and the hyperbolic excess velocity,  $v_\infty = \sqrt{-\mu/a}$ .

<sup>1</sup> We examined the final eccentricity distributions of the simulated planets, which were slightly broader than those observed — consistent with expectations from the point-mass approximation, which enhances the dynamical heating of giant planets.



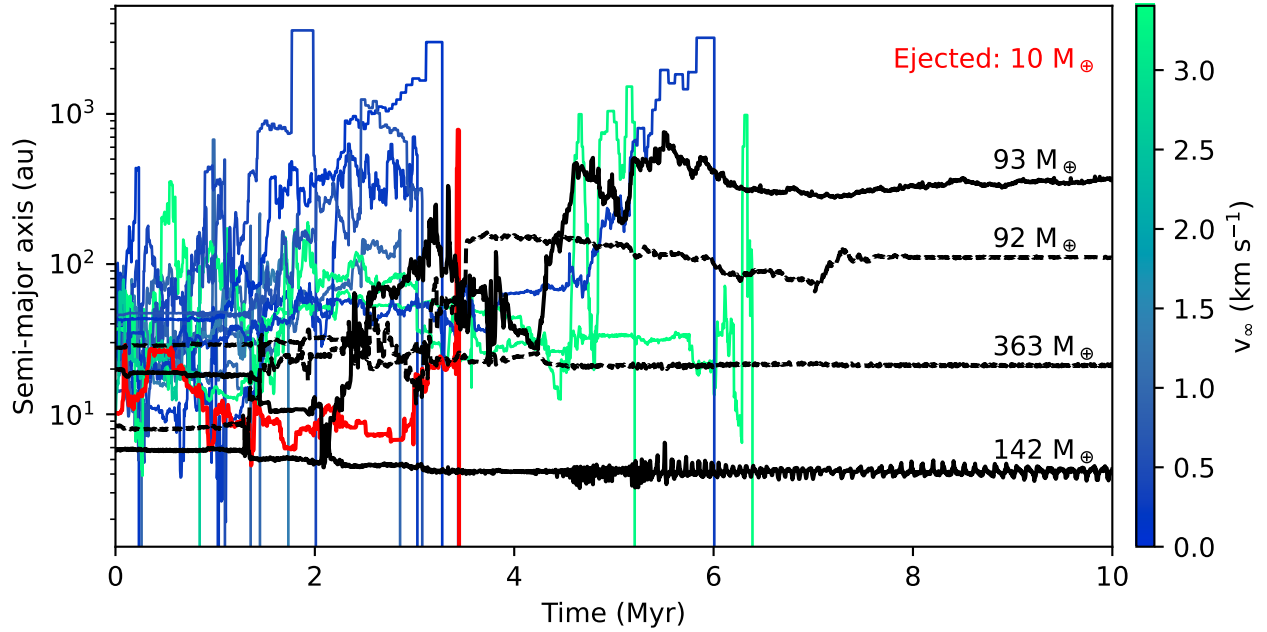


FIG. 3.— Semi-major axis time series for planets and 16 randomly chosen ejected planetesimals in the example system. Colours from blue to green indicate ejection velocity magnitude for ISOs. The red curve shows the ejected  $10 M_{\oplus}$  planet; black curves show planets that remain bound at 10 Myr.

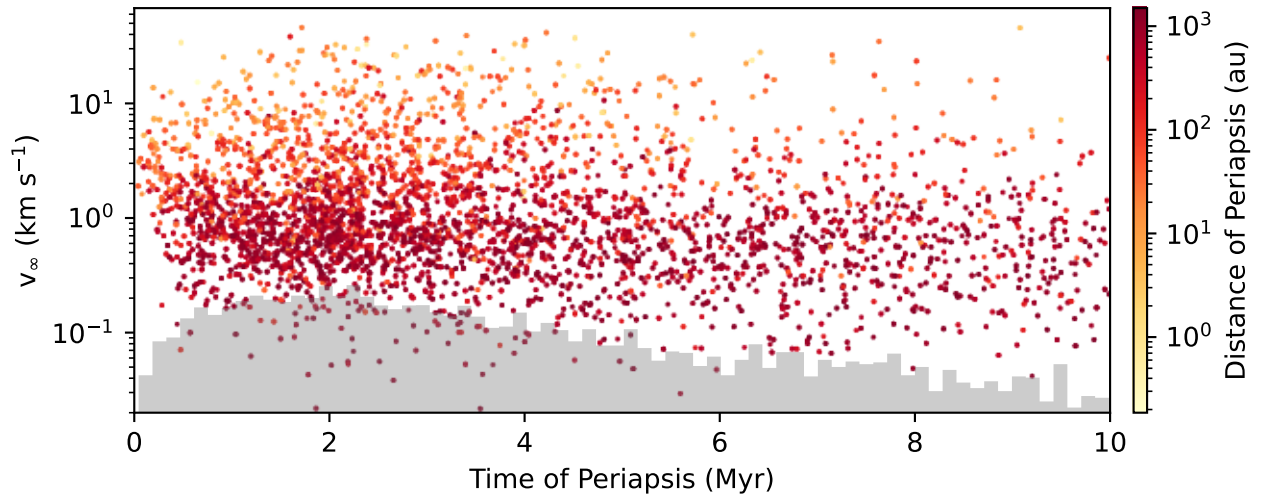


FIG. 4.— Ejection time, perihelion distance, and velocity for all ISOs in the example system. Early ejections ( $t < 2$  Myr) from inner regions show the highest velocities. Ejection velocity decreases with perihelion distance. The grey histogram shows the ejection flux, which peaks at 2 Myr after simulation initialisation, and then steadily decreases.

### 3. RESULTS

#### 3.1. Individual System Analysis

Individual system evolution reveals physical mechanisms that population statistics alone cannot capture. We first present detailed results from a representative example simulation, illustrating the mechanisms we then quantify statistically in subsection 3.2. The example simulation contains five planets with a total initial planetary mass of  $700 M_{\oplus}$ . The system has a median  $v_{\infty} = 2.31 \text{ km s}^{-1}$ , and the fraction of ejected planetesimals is 0.664.

Figure 3 shows the time evolution of the planetary semi-major axes alongside 16 randomly-selected ejected particles. The system undergoes a catastrophic instability early in its evolution. Most planets experience significant orbital changes, and one  $10 M_{\oplus}$  planet is ejected. The planet trajectories also indicate that mass asymmetry drives instability outcomes, with the largest planets remaining stable, and the smaller planets ejected or scattered onto high semi-major axis orbits. ISOs are ejected through two main pathways. Some experience single strong scattering events that directly impart hyperbolic velocities, while others undergo gradual outward diffusion in semi-major axis before gentle unbinding. The majority of the shown ISOs are ejected in the first two Myr of the simulation, as seen in the ejection

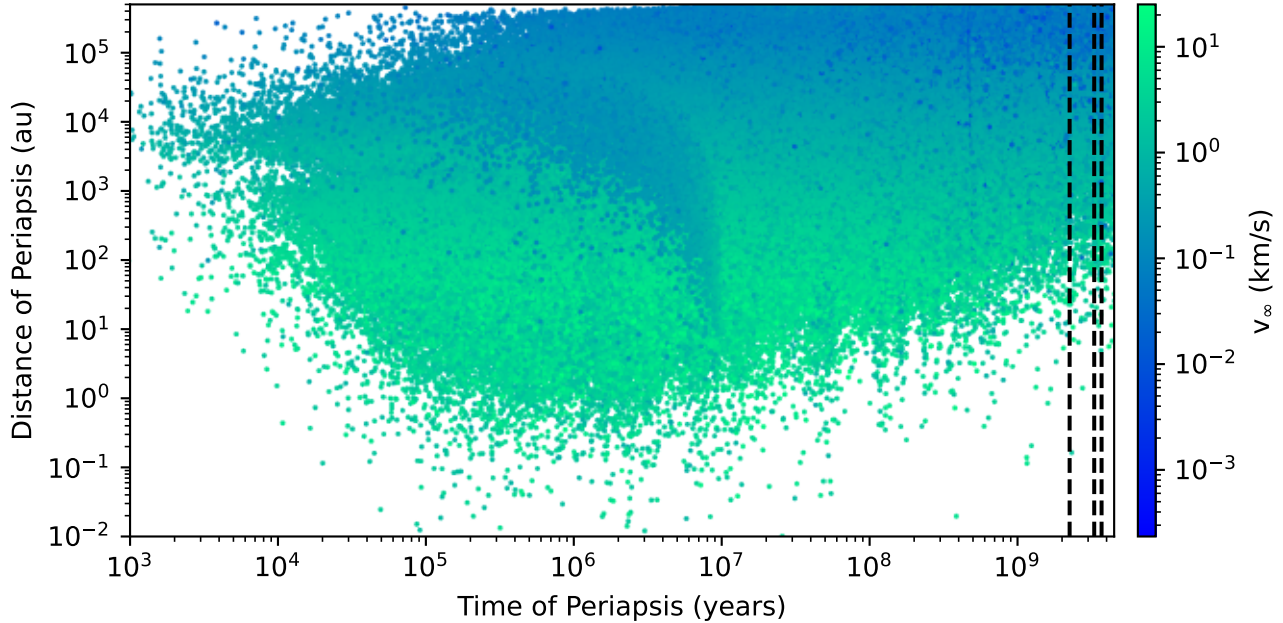


FIG. 5.— Temporal evolution of ISO ejection velocities in the Solar System simulation of N23. Each point shows an ejected particle’s  $v_\infty$  at the time of ejection, calculated from its orbital elements at 500,000 au and traced back to perihelion passage time. Colour indicates perihelion distance, while vertical dashed lines correspond to strong stellar flyby events that perturb the system. Additional vertical features may indicate further stellar encounters.

flux shown in the gray histogram of Figure 4. The early flux increase may reflect either the planetary instability or relaxation of initially unstable planetesimal orbits. This plot also shows which regions of the planetesimal disc contribute most to the ejected population, with the majority of ejected objects having a perihelion exceeding that of the planets at any given time. Planetesimals located farther from the star at the time of ejection are ejected with lower  $v_\infty$ , as expected for weakly bound, slower-moving orbits. Low-velocity, distant ejections become more dominant later in the integration. This pattern suggests that early ejections are dominated by close encounters near the planets, while later ones arise from more gradual diffusion of distant planetesimals.

The system’s velocity distribution evolves as inner planetesimals are preferentially depleted early. The median  $v_\infty$  peaks at  $3.0 \text{ km s}^{-1}$  during the initial instability ( $\sim 0.25 \text{ Myr}$  after the start of the simulation), then declines to a plateau of  $0.9 \text{ km s}^{-1}$  by 10 Myr. This behaviour parallels the Solar System evolution seen in N23, though with lower velocities (the Solar System simulation has  $8.0 \text{ km s}^{-1}$  peak and  $1.0 \text{ km s}^{-1}$  plateau). A diffusion timescale is required for particles to migrate onto orbits large enough to be gently ejected at low velocities. This is evident in Figure 5, where the maximum perihelion distance increases throughout the 4.5 Gyr integration. Particles were removed at 500,000 au barycentric distance; the upper envelope in perihelion distance reflects this removal threshold combined with orbital eccentricity. Additionally, these ejections are the slowest ( $< 10^{-3} \text{ km s}^{-1}$ ), leading to a gradual build-up of the low-velocity tail of the distribution. The low-velocity tail is also sensitive to physical effects not included in our simulations. We omit both stellar flybys and Galactic tides: the former can generate slow-moving ISOs (Pfalzner et al. 2021), and the latter plays an important role in shaping Oort-cloud dynamics (Fernández 1997), where planetesimals’ Keplerian velocities are much lower than in the planetary region. Finally, our 10 Myr integrations may be too short for planetesimals originating near the outer disk edge (40 au) to diffuse onto the high-eccentricity, distant orbits required for such low-velocity ejections.

The inclination distribution of ejected ISOs, shown in Figure 6, provides a kinematic fingerprint of the underlying ejection mechanism. The distribution is strongly anisotropic and prograde-dominated, with most ISOs ejected at low inclinations. The absence of planetesimal self-stirring in our simulations likely accentuates this planar bias. Self-gravitating debris discs develop enhanced inclination dispersion through collective effects. This would seed a broader range of initial inclinations, producing more isotropic high-velocity ejections. Direct comparison of the ejection inclination distributions from our system with N23 is difficult. The Galactic tide significantly alters the non-radial component of the velocity of ejected objects from the ejection point to the measurement at 500,000 au. To compare the inclination distributions, we instead plot the Galactic latitude and longitude of the ISO ejections from our system and N23, centred on the barycentre of the system, shown in Figure 7 and oriented around the invariant plane of the system. Both systems show strong concentration toward the invariant plane, with the N23 particles reproducing the expected pattern from the effects of the Galactic tide.

The individual system analysis demonstrates that ISO production efficiency and ejection kinematics vary systematically with planetary architecture and evolutionary phase. For ensemble-level analysis, we therefore focus on two complementary metrics: the ejected fraction (total ISOs produced relative to the initial planetesimal population) and

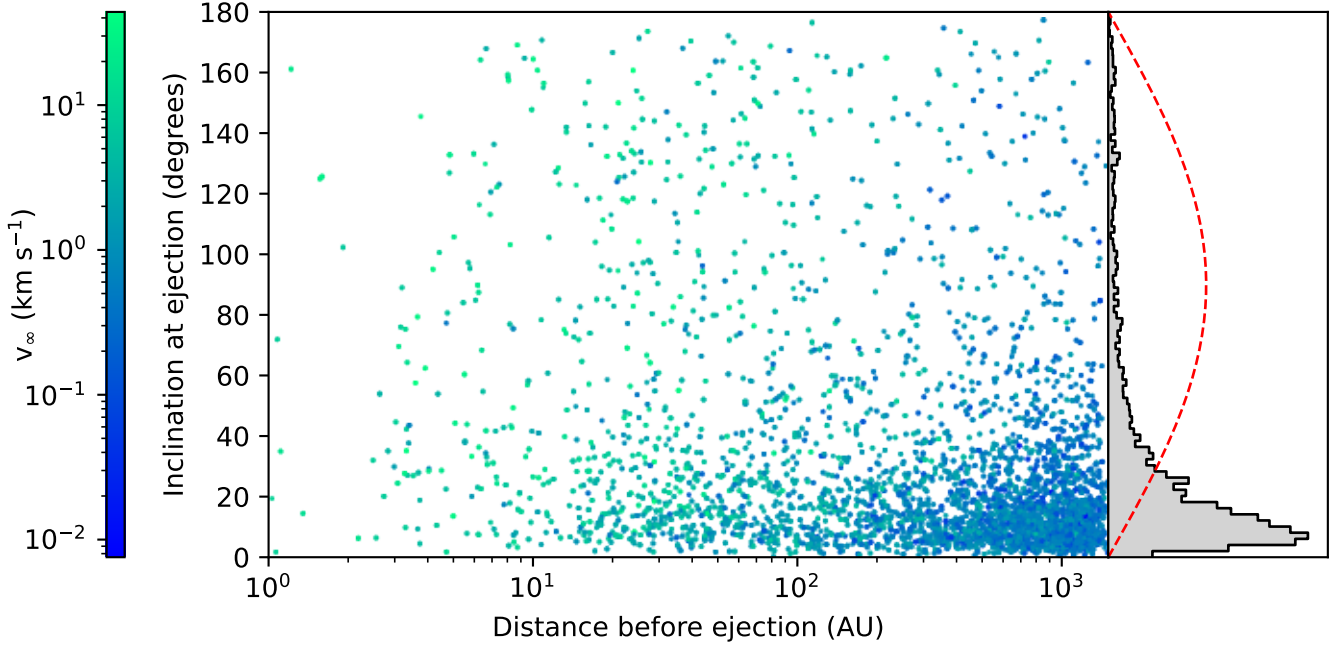


FIG. 6.— Inclinations of ISOs ejected from the example system. The fraction of low inclination ejections increases with respect to distance from the star. Most ejections remain at low inclination. The red dashed line shows the distribution expected for isotropic ejections.

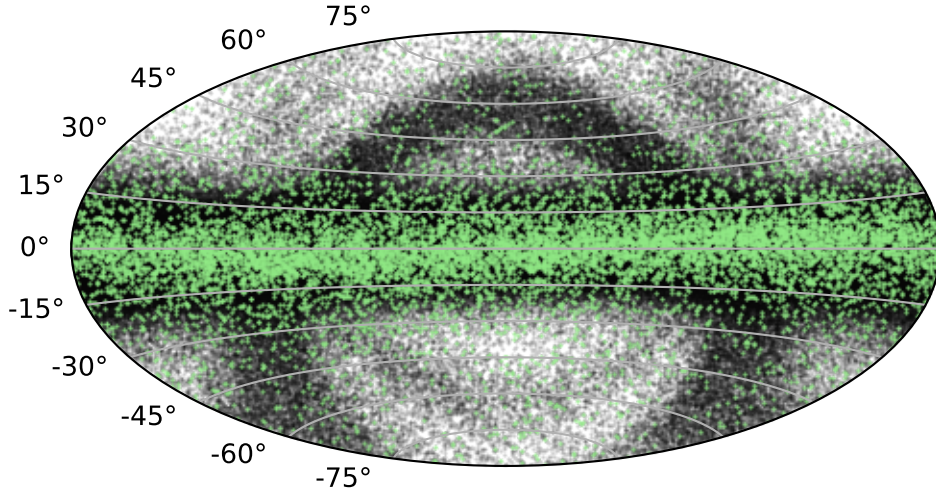


FIG. 7.— Galactic latitude and longitude of ejected particles. Black points are from N23 over the whole 4.5 Gyr of the simulation, and green points show our example simulation after 10 Myr. The majority of ejected ISOs are in the ecliptic, with the particles from N23 showing the effects of integration in the Galactic tide and flybys. Particles from both simulations decrease in density at greater latitudes.

the median ejection velocity  $v_\infty$ . The ejected fraction quantifies system-to-system variability in ISO production efficiency, while median  $v_\infty$  characterizes the typical kinematic signature. We use the median rather than mean because it is robust to rare high-velocity outliers from close encounters.

### 3.2. Simulation Ensemble Analysis

The ensemble of 2,461 completed simulations reveals bimodality in ISO production outcomes. In the median  $v_\infty$ –ejection fraction plane (Figure 8), systems segregate into an L-shaped distribution comprising two distinct branches. The vertical lobe spans a wide range of ejection fractions ( $\lesssim 0.7$ ) while maintaining relatively modest median velocities ( $\sim 1\text{--}2\text{ km s}^{-1}$ ). The horizontal lobe, by contrast, clusters at elevated ejection fractions ( $\gtrsim 0.4$ ) and exhibits higher median velocities ( $\sim 2\text{--}5\text{ km s}^{-1}$ ). This bimodality reflects two fundamentally different modes of planetesimal disc dispersal: gentle, protracted ejection driven by weak secular perturbations, and violent ejection accompanying global dynamical instabilities.

The full velocity distributions for 80 randomly selected simulations are shown in Figure 9, coloured consistently

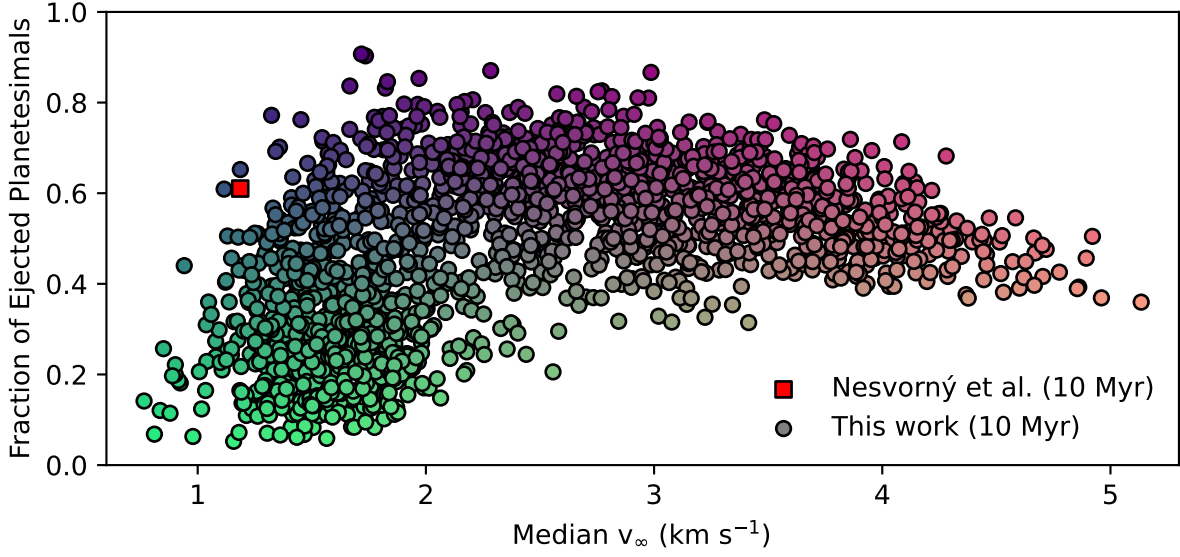


FIG. 8.— Summary statistics for all 2,461 simulated systems: fraction of planetesimals ejected versus the median  $v_\infty$  of ejected particles. Colour encodes position in this parameter space for identification in subsequent figures. The red square marks the Solar System value from N23 including all particles that have reached 500,000 au, and that have pericentre passage times earlier than 10 Myr. Over time, the N23 point would move up and to the left as slower particles unbound from the Oort cloud contribute to the velocity distribution.

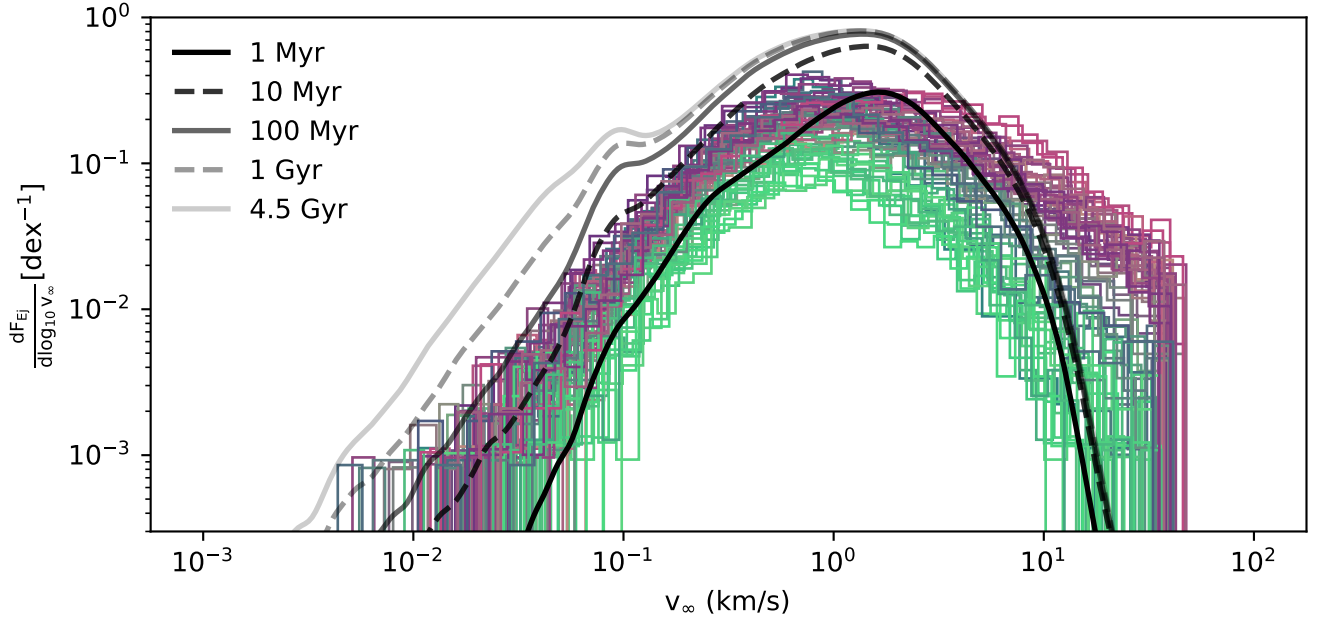


FIG. 9.— The  $v_\infty$  distributions for 80 randomly selected simulations, coloured according to their positions in Figure 8. Black and gray curves show the Solar System ejection velocity distributions from N23 at different times. For example, “10 Myr” refers to ejected particles from N23 that reach 500,000 au with pericentre passage times  $\tau < 10$  Myr.

with their positions in the median  $v_\infty$ -ejection fraction plane. For comparison, we also include the ejection-velocity distributions from the N23 Solar System integration at several evolutionary snapshots. At 10 Myr (our maximum integration time), the Solar System’s  $v_\infty$  distribution has a similar peak and width to those of our systems, most closely resembling the distributions in the lower-left region of Figure 8 (green histograms). The higher-velocity tail in our simulations likely reflects two factors: the omission of collision handling (which would otherwise damp extreme scattering outcomes) and the higher mass budgets in our models compared to the Solar System, both of which increase the frequency and energy of strong scattering events. By 100 Myr, the N23 Solar System simulation develops a pronounced low-velocity tail. This less-numerous late-emerging population arises from the gradual stripping of the extended Oort Cloud through a combination of weak planetary perturbations, Galactic tides, and passing stars. Our simulations, which omit these external perturbations and conclude at 10 Myr, do not reproduce this feature. Its absence highlights a key difference in scope: our ISO populations represent the bodies produced by dynamical instability within



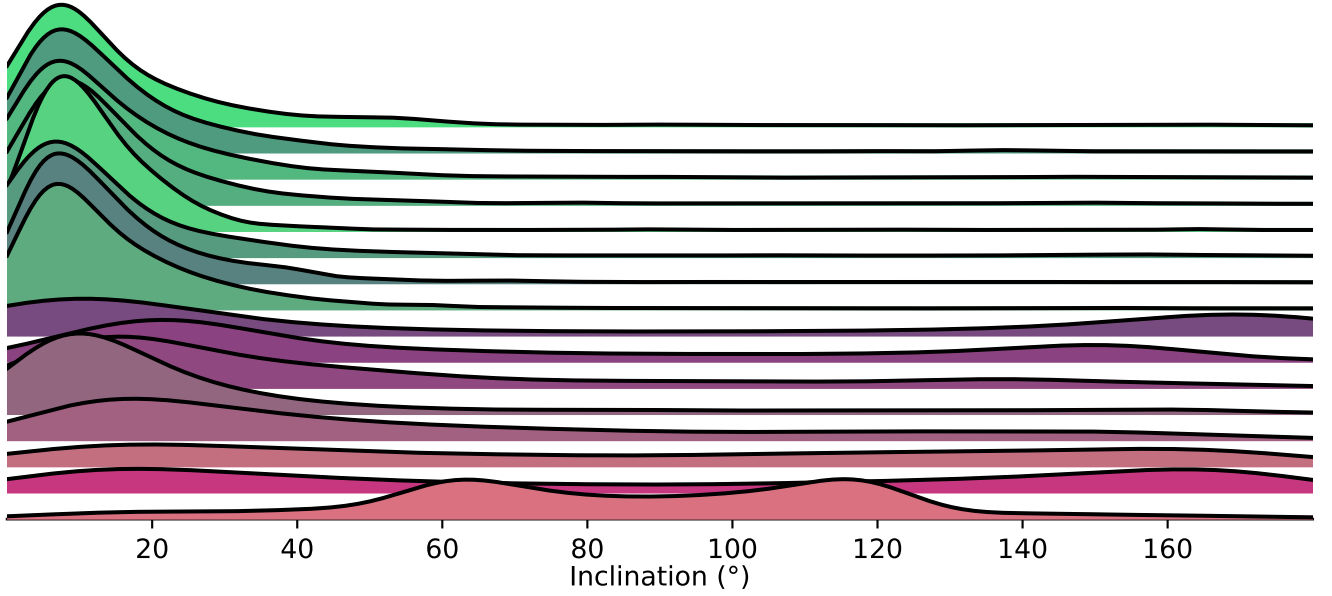


FIG. 10.— Inclination distribution of ejected ISOs of 25 randomly selected simulations, coloured according to their positions in Figure 8. Green-coloured systems predominantly have prograde low-inclination ejections. The systems with the highest ejection velocities display more extreme inclination distributions.

TABLE 1  
DEFINITIONS OF SYSTEM ARCHITECTURE PARAMETERS, AS USED IN THIS WORK. FOR FULL EXPLANATIONS, SEE GILBERT & FABRYCKY (2020).

Parameter	Name	Definition	Meaning
$N$	Multiplicity	$N$	Number of planets in the system.
$\mathcal{Q}$	Mass Partitioning	$\left(\frac{N}{N-1}\right) \sum_{i=1}^N \left(m_i^* - \frac{1}{N}\right)^2$	Ranges from 0 to 1. $\mathcal{Q} = 0$ means equal masses; $\mathcal{Q} = 1$ means all the mass is in one planet.
$\mathcal{M}$	Monotonicity	$\rho_s \mathcal{Q}^{1/N}$	Ranges from $-1$ to $1$ . Positive means mass increases with semi-major axis.
$\mathcal{C}$	Gap Complexity	$-K \sum_{i=1}^n p_i^* \log(p_i^*) \left(p_i^* - \frac{1}{n}\right)^2$	$\mathcal{C} = 0$ for evenly spaced planets in log-period; $\mathcal{C} = 1$ when one spacing dominates.
$\mathcal{S}$	Characteristic Spacing	$\text{mean}(\Delta_H)$	Average spacing in mutual Hill radii.
$M$	Total Mass	$\sum_{i=1}^N m_i$	Total planetary mass.

NOTE. — [1]  $m_i^* = \frac{m_i}{\sum_i m_i}$ . [2]  $p_i^* = \frac{\log(P'/P)}{\log(P_{\max}/P_{\min})}$ . [3]  $\Delta_H = \frac{a' - a}{r_H}$ , with  $r_H = \left(\frac{m' + m}{3}\right)^{1/3} \left(\frac{a' + a}{2}\right)$ .

planetary systems, not those generated by longer-term, stripping processes.

We also examined the inclination distribution across the simulation ensemble. Figure 10 shows 25 systems selected from across the parameter space. There are major structural differences in the inclination distributions depending on their position in the median  $v_\infty$ -ejection fraction plane. The lowest ejection fraction systems (green) primarily have prograde ejections, with relatively low inclinations, displaying strongly asymmetric distributions. The intermediate (purple) systems have broader distributions. The majority of ejections remain prograde, with higher typical inclinations than green systems. Many purple systems show bimodal distributions, with a second peak of high inclination (prograde) ejections. Orange systems often show bimodal distributions with peaks near  $90^\circ$ . This reflects increasing energy of scattering events as systems move up and across the median  $v_\infty$ -ejection fraction plane. None of the systems produce isotropic ejection distributions.

To assess the information about system architecture that is contained in the ISO velocity distributions, we investigated correlations between ejection outcomes and planetary configuration metrics. For this purpose, we adopted a slightly modified version of the exoplanet architecture classification scheme introduced by Gilbert & Fabrycky (2020). Definitions of the architecture parameters are provided in Table 1, with the derivations and motivation discussed in detail by Gilbert & Fabrycky (2020). Figure 11 and Figure 12 show the  $v_\infty$ -ejection fraction plane, coloured by system architecture parameters. Each parameter is shown at three epochs: initial (left), final after 10 Myr (middle), and net change (right). We then used  $k$ -means clustering to quantify whether the two lobes correspond to distinct system architectures.

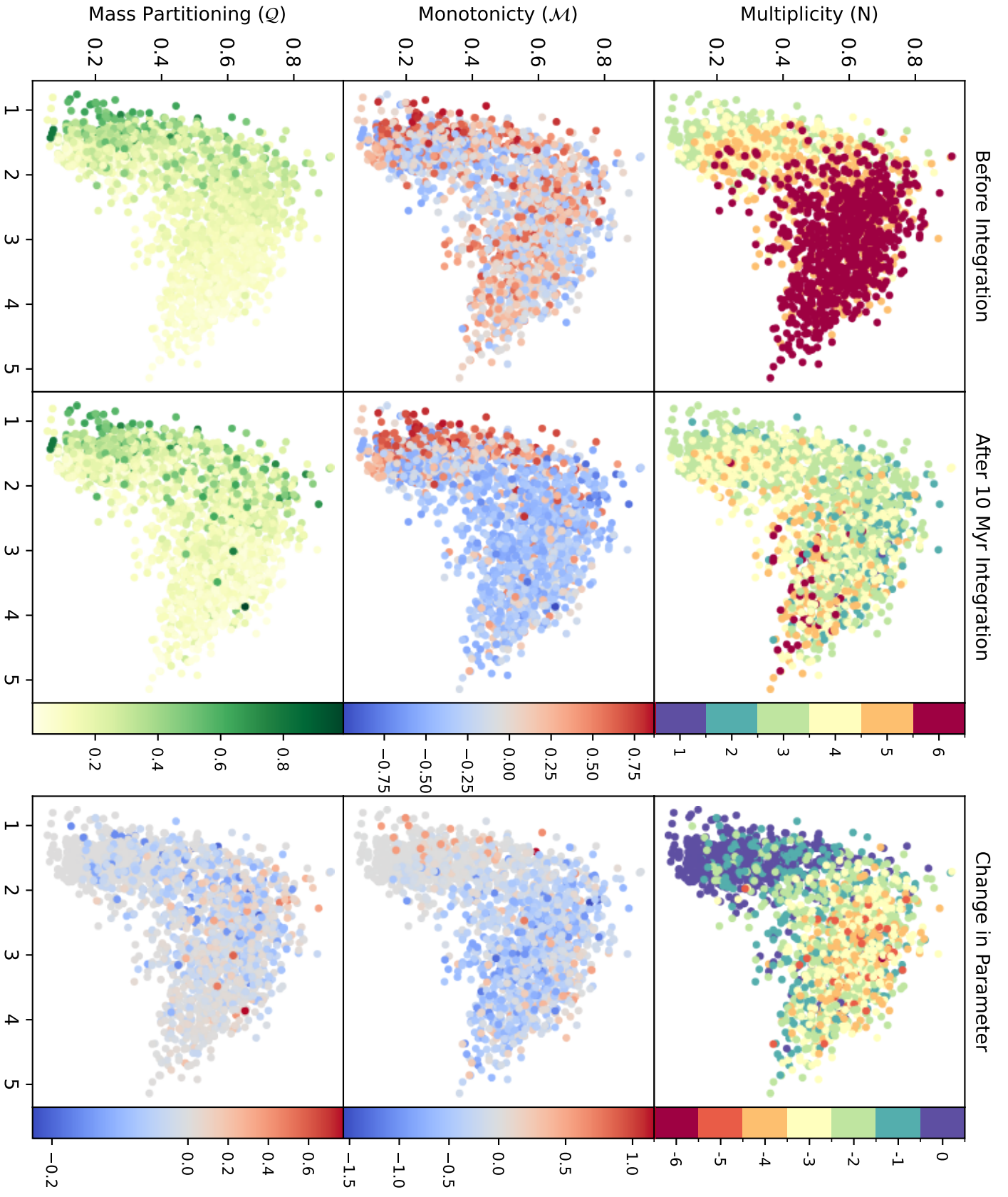


FIG. 11.— Scatter plots of ISO outcomes coloured by selected system architecture parameters, measured for all simulated systems. Left: initial values; Middle: final values; Right: net change, defined as the final minus initial value.

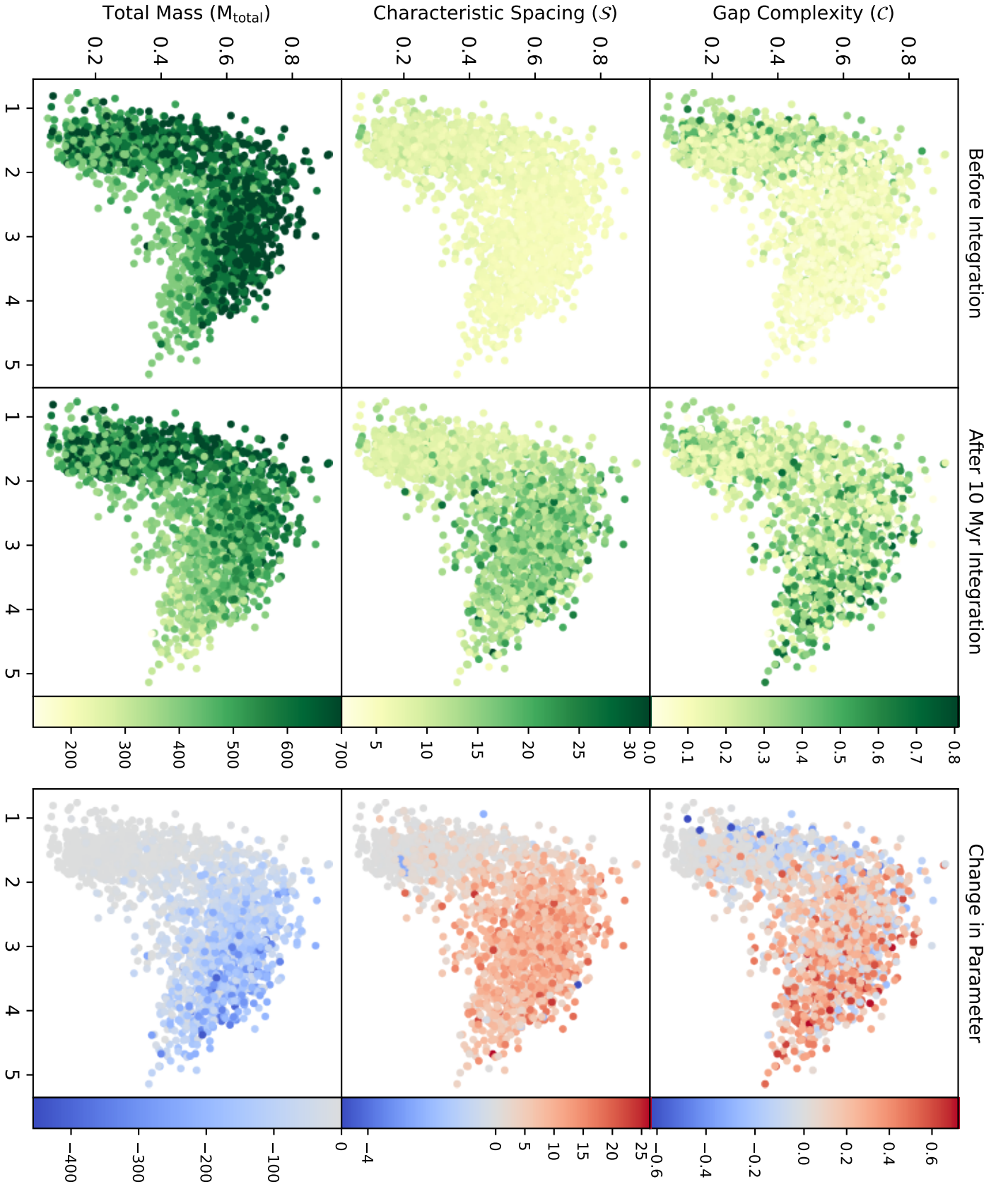


Fig. 12.— Same as Figure 11, for the remaining architecture parameters.

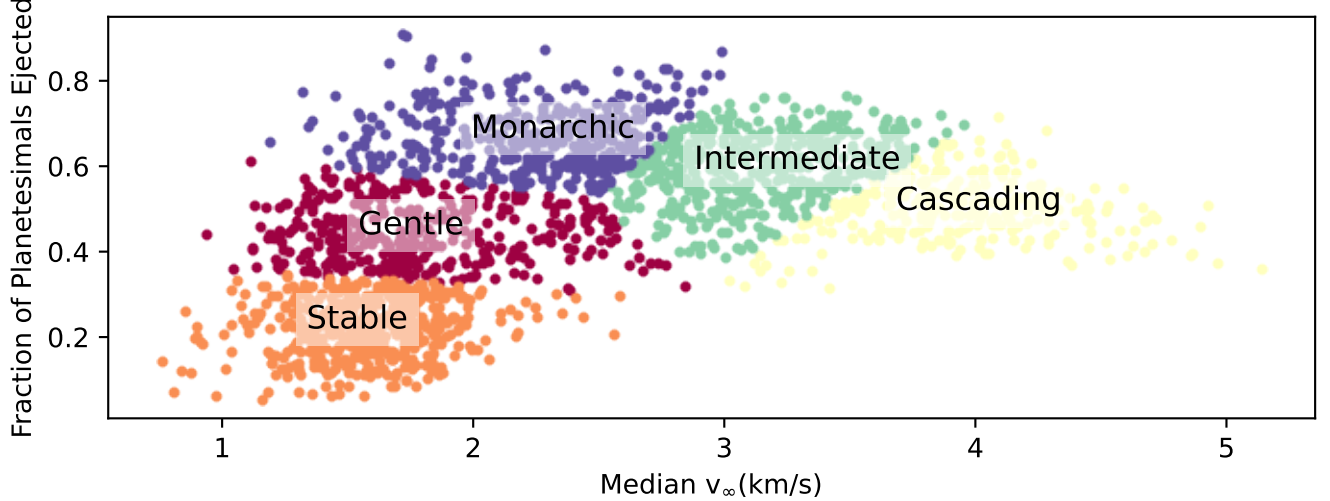


FIG. 13.— Separation of systems into 5 sub-clusters based on their location in the  $v_\infty - f_{ej}$  plane. The *quiet evolution* cluster is essentially composed of the gentle and stable regions, and the *catastrophic evolution* cluster is composed of the monarchic, intermediate and cascading sub-clusters.

### 3.3. Clustering

The results of the  $k$ -means clustering are shown in Figure 13, and the parameter distributions for each cluster are summarised in Table 2. We first used  $k = 2$  to isolate the dominant two-mode structure in the  $v_\infty - f_{ej}$  plane, which has an “L”-shaped morphology. In all cases, clustering was performed in the  $v_\infty - f_{ej}$  parameter space, where each dimension was standardised to have a mean of zero and variance of one. The clustering then used a Euclidean distance metric in this standardised space. We assigned the descriptive labels *catastrophic evolution* to the high-velocity horizontal branch and *quiet evolution* to the low-velocity vertical branch. To investigate what drives the transition from the green to the orange regions of the plot, we clustered with  $k = 5$ , which essentially further subdivided the *quiet evolution* cluster into two sub-clusters and the *catastrophic evolution* branch into three additional sub-clusters.

### 3.4. Cluster System Architecture Trends

Systems in the catastrophic evolution cluster are marked by violent dynamical activity, ejecting many high-speed ISOs and often losing several planets. By contrast, quiet evolution systems remain comparatively calm, showing smaller orbital rearrangements and ejecting fewer planets.

The most significant system architectural features of catastrophic systems are large increases in characteristic spacing, with planets spreading apart by an average of 8.237 mutual Hill radii. These systems also experience substantial mass loss, with a median loss of 89.4  $M_\oplus$ . They undergo significant reductions in multiplicity, losing a median of 2 planets per system, confirming that planet ejection is a common occurrence in these systems. Monotonicity also typically increases ( $\Delta\mathcal{M} = 0.296$ ), consistent with preferential removal of lower-mass planets or inward scattering.

The quiet systems, in contrast, retain much of their initial architecture. They lose very little mass (most systems ejecting no planets), and experience only minor changes in characteristic spacing (0.028 mutual Hill radii). They begin with higher gap complexities, with a median of 0.219. Wider initial spacing allows more irregular planet placement during initialization, increasing gap complexity. Quiet systems also show higher initial mass partitioning, 0.196, (catastrophic systems,  $\mathcal{Q} = 0.118$ ), meaning they are hosting planets with more asymmetric masses. Lower multiplicities make asymmetric mass distributions more likely, due to the  $\alpha = 1$  parametrisation of the Dirichlet distribution. The mass asymmetry in quiet systems likely suppresses chaotic multi-body interactions, providing a stabilizing influence. Most quiet systems preserve their initial monotonicity, indicating limited planetary reordering and ejections.

Both clusters converge to a median final multiplicity of three planets and have similar final total masses (500  $M_\oplus$  and 449  $M_\oplus$ ). This configuration appears to be a dynamically stable outcome for the high-mass architectures explored here. Within the broader catastrophic and quiet groups, we further explored dividing the simulations into finer structure: three catastrophic sub-clusters and two quiet sub-clusters. Although this five-way division was guided by the elbow method for  $k$ -means clustering, the choice is still somewhat arbitrary. Our goal in subdividing the parameter space was to identify architectural commonalities within each region, rather than to claim that the data naturally separate into five intrinsic classes. These classes may not translate to systems with different mass-multiplicity regimes. The average system-architecture parameters for each sub-cluster are listed in Table 3. Together, these subdivisions reveal a continuum of dynamical pathways and show how planetary architecture modulates ISO production.

#### 3.4.1. Quiet Sub-Clusters

The quiet evolution cluster was divided into two sub-populations, separated at an ejection fraction of  $\sim 0.3$ . Although both sub-clusters exhibit similar median  $v_\infty$  values (1.594 and 1.737  $\text{km s}^{-1}$ ), their ejection fractions differ substantially (0.227 to 0.435), motivating this distinction.



TABLE 2

PERCENTILE SUMMARY OF SYSTEM ARCHITECTURE PARAMETERS FOR THE TWO MAIN CLUSTERS. VALUES CORRESPOND TO THE 16TH, 50TH, AND 84TH PERCENTILES OF EACH POPULATION, AT THE BEGINNING OF THE SIMULATION (INITIAL), THE END OF 10 MYR OF EVOLUTION (FINAL), AND THEIR DIFFERENCE, FINAL MINUS INITIAL (CHANGE). THE 16TH AND 84TH PERCENTILE COLUMNS ARE DE-EMPHASIZED FOR CLARITY.

Parameter	Quiet			Catastrophic		
	16%	50%	84%	16%	50%	84%
<b>Summary</b>						
Number of simulations		<b>777</b>			<b>1184</b>	
$v_{\infty, \text{med}}$ (km s <sup>-1</sup> )	1.345	<b>1.611</b>	1.871	2.205	<b>2.927</b>	3.754
Fraction ejected	0.171	<b>0.284</b>	0.430	0.485	<b>0.593</b>	0.688
<b>Initial</b>						
Multiplicity	3	<b>4</b>	5	5	<b>6</b>	7
Mass Partitioning	0.071	<b>0.196</b>	0.385	0.063	<b>0.118</b>	0.216
Monotonicity	-0.420	<b>-0.042</b>	0.502	-0.298	<b>-0.019</b>	0.378
Gap Complexity	0.130	<b>0.219</b>	0.368	0.057	<b>0.104</b>	0.186
Characteristic Spacing	6.775	<b>8.246</b>	9.931	5.156	<b>5.946</b>	6.916
Total Mass (M <sub>⊕</sub> )	400	<b>500</b>	700	400	<b>600</b>	700
<b>Final</b>						
Multiplicity	3	<b>3</b>	4	3	<b>3</b>	4
Mass Partitioning	0.061	<b>0.168</b>	0.367	0.036	<b>0.112</b>	0.225
Monotonicity	-0.453	<b>-0.078</b>	0.513	-0.511	<b>-0.356</b>	-0.090
Gap Complexity	0.128	<b>0.225</b>	0.369	0.050	<b>0.261</b>	0.496
Characteristic Spacing	7.605	<b>9.101</b>	11.361	10.603	<b>14.279</b>	19.057
Total Mass (M <sub>⊕</sub> )	400	<b>500</b>	692	351	<b>449</b>	570
<b>Change</b>						
Multiplicity	-1	<b>0</b>	0	-3	<b>-2</b>	-1
Mass Partitioning	-0.040	<b>0.000</b>	0.000	-0.055	<b>0.003</b>	0.047
Monotonicity	-0.104	<b>0.000</b>	0.002	-0.662	<b>0.296</b>	0.004
Gap Complexity	-0.026	<b>-0.000</b>	0.021	-0.080	<b>0.1482</b>	0.394
Characteristic Spacing	-0.024	<b>0.028</b>	2.648	4.233	<b>8.237</b>	13.187
Total Mass (M <sub>⊕</sub> )	-10.6	<b>0.000</b>	0.000	-188.0	<b>-89.4</b>	-31.0

TABLE 3

PERCENTILE SUMMARY OF SYSTEM ARCHITECTURE PARAMETERS FOR THE FIVE SUB-CLUSTERS. VALUES CORRESPOND TO THE 16TH, 50TH, AND 84TH PERCENTILES OF EACH POPULATION AT THE BEGINNING OF THE SIMULATION (INITIAL), THE END OF 10 MYR OF EVOLUTION (FINAL), AND THEIR DIFFERENCE, FINAL MINUS INITIAL (CHANGE). THE 16TH AND 84TH PERCENTILE COLUMNS ARE DE-EMPHASISED FOR CLARITY.

Parameter	Stable			Gentle			Monarchic			Intermediate			Cascading		
	16%	50%	84%	16%	50%	84%	16%	50%	84%	16%	50%	84%	16%	50%	84%
<b>Summary</b>															
Number of Simulations		<b>491</b>			<b>358</b>			<b>386</b>			<b>457</b>			<b>269</b>	
$v_{\infty, \text{med}}$ (km s <sup>-1</sup> )	1.320	<b>1.594</b>	1.837	1.411	<b>1.737</b>	2.250	1.833	<b>2.293</b>	2.578	2.812	<b>3.092</b>	3.454	3.551	<b>3.902</b>	4.290
$f_{\text{ej}}$	0.146	<b>0.227</b>	0.295	0.368	<b>0.435</b>	0.518	0.595	<b>0.659</b>	0.741	0.514	<b>0.597</b>	0.672	0.426	<b>0.497</b>	0.565
<b>Initial</b>															
Multiplicity	3	<b>3</b>	4	3	<b>4</b>	6	4	<b>5</b>	7	5	<b>6</b>	7	5	<b>6</b>	7
Mass Partitioning	0.07	<b>0.20</b>	0.43	0.08	<b>0.18</b>	0.33	0.13	<b>0.19</b>	0.28	0.07	<b>0.10</b>	0.16	0.03	<b>0.07</b>	0.11
Monotonicity	-0.43	<b>-0.03</b>	0.52	-0.38	<b>-0.09</b>	0.39	-0.29	<b>0.00</b>	0.50	-0.33	<b>-0.06</b>	0.36	-0.22	<b>0.03</b>	0.33
Gap Complexity	0.13	<b>0.23</b>	0.38	0.10	<b>0.19</b>	0.32	0.07	<b>0.13</b>	0.24	0.06	<b>0.10</b>	0.18	0.05	<b>0.08</b>	0.14
Characteristic Spacing	7.07	<b>8.60</b>	10.29	6.17	<b>7.46</b>	8.99	5.19	<b>6.12</b>	7.03	5.06	<b>5.82</b>	6.79	5.23	<b>5.87</b>	6.70
Total Mass (M <sub>⊕</sub> )	400	<b>500</b>	600	400	<b>600</b>	700	500	<b>600</b>	700	400	<b>600</b>	700	400	<b>500</b>	600
<b>Final</b>															
Multiplicity	3	<b>3</b>	4	3	<b>3</b>	4	2	<b>3</b>	4	2	<b>3</b>	4	3	<b>4</b>	5
Mass Partitioning	0.07	<b>0.18</b>	0.38	0.05	<b>0.16</b>	0.30	0.08	<b>0.18</b>	0.35	0.03	<b>0.09</b>	0.18	0.03	<b>0.07</b>	0.13
Monotonicity	-0.46	<b>-0.05</b>	0.53	-0.47	<b>-0.24</b>	0.34	-0.53	<b>-0.37</b>	0.05	-0.50	<b>-0.36</b>	-0.13	-0.48	<b>-0.32</b>	-0.07
Gap Complexity	0.13	<b>0.22</b>	0.37	0.12	<b>0.22</b>	0.35	0.00	<b>0.23</b>	0.43	0.00	<b>0.28</b>	0.51	0.12	<b>0.33</b>	0.55
Characteristic Spacing	7.60	<b>8.98</b>	11.00	7.84	<b>9.60</b>	13.63	10.46	<b>14.35</b>	18.45	11.57	<b>15.19</b>	19.45	9.85	<b>13.37</b>	18.61
Total Mass (M <sub>⊕</sub> )	400	<b>500</b>	600	400	<b>528</b>	692	430	<b>528</b>	632	357	<b>443</b>	532	294	<b>363</b>	420
<b>Change</b>															
Multiplicity	-1	<b>0</b>	0	-2	<b>-1</b>	0	-3	<b>-2</b>	-1	-4	<b>-2</b>	-1	-3	<b>-2</b>	-1
Mass Partitioning	-0.02	<b>0.00</b>	0.00	-0.07	<b>0.00</b>	0.00	-0.07	<b>0.00</b>	0.07	-0.05	<b>0.01</b>	0.04	-0.03	<b>0.00</b>	0.03
Monotonicity	0.00	<b>0.00</b>	0.00	-0.01	<b>0.00</b>	0.00	-0.65	<b>-0.29</b>	-0.03	-0.69	<b>-0.29</b>	-0.05	-0.65	<b>-0.34</b>	-0.03
Gap Complexity	-0.01	<b>0.00</b>	0.01	-0.09	<b>0.00</b>	0.15	-0.11	<b>-0.08</b>	0.31	-0.06	<b>-0.17</b>	0.40	0.00	<b>0.25</b>	0.47
Characteristic Spacing	-0.04	<b>-0.01</b>	1.29	0.00	<b>-1.73</b>	6.67	3.65	<b>8.28</b>	12.4	5.45	<b>9.33</b>	13.9	3.81	<b>7.52</b>	12.78
Total Mass (M <sub>⊕</sub> )	-2.0	<b>0.0</b>	0.0	-43.3	<b>1.45</b>	0.0	-143.5	<b>-76.7</b>	-26.0	-211.3	<b>-106.3</b>	-43.5	-215.9	<b>-108.2</b>	-32.9

We refer to the lower-ejection fraction systems as *stable systems*. These systems are not entirely static, but their architecture parameters change far less than in other clusters. For every parameter, the mean change is near zero. These systems have the highest initial gap complexity (0.23), which remains nearly constant, and the largest characteristic spacings (8.60 initially, increasing to 8.98 mutual Hill radii). This indicates that these systems are sparsely populated with planets initially, and unlikely to experience dynamical instabilities. The monotonicity also shows negligible change, indicating no reordering of planetary masses. These properties suggest that stable systems do not undergo large-scale orbital changes. They also begin with low multiplicities (median 3) and have a median of zero planetary ejections, reinforcing the picture of long-lived, sparsely-populated planetary architectures. The typical ejected bodies from these systems are small, with the upper 84% boundary at a mass loss of  $2 M_{\oplus}$ , and most commonly no planets are ejected. As a result, these systems eject few ISOs, and those that do escape are likely removed through gentle unbinding or single scattering events, which can only experience a finite velocity kick of  $v_{\text{esc}}/\sqrt{2}$  (Wyatt et al. 2017).

The second sub-cluster, which we term the *gentle ejectors*, exhibits more dynamical activity while still avoiding catastrophic disruption. Compared to the stable systems, these have slightly higher initial multiplicities (4) and starting masses ( $600 M_{\oplus}$ ), and lose on average 1 planet over the integration. Their characteristic spacings grow from a median 7.46 to 9.6, larger than in the stable systems but far below the final spacings of  $\sim 14$  attained by catastrophic systems. This indicates that the orbits of planets in gentle ejector systems expand outward, but remain relatively tightly packed at the end of the evolution. Gap complexity and monotonicity changes are minimal, reinforcing the picture of limited reordering. Their higher median starting masses ( $600 M_{\oplus}$ ) and relatively small mass loss ( $1 M_{\oplus}$ ) lead to these systems retaining the largest amount of mass (although strongly overlapping with the monarchic ejector sub-cluster). We interpret this as evidence that most planets remain bound, and that these systems produce ISOs largely through gradual orbital evolution rather than direct ejection by planets. Planet–planetesimal interactions slowly modify small-body orbits, lifting them onto unstable trajectories over long timescales. The ISO flux in the time-frame we examine is therefore driven less by impulsive scattering events and more by cumulative orbital changes. This highlights that significant ISO production within 10 Myr does not necessarily require strong, violent instabilities, but can also emerge from comparatively quiescent dynamical pathways. Both of the quiet clusters release ISOs at similar velocities, so within the 10 Myr timescale the more massive gentle ejector systems are able to eject more material due to their higher starting masses, but through a similar process as the stable systems.

### 3.4.2. Catastrophic Sub-Clusters

For the  $k = 5$  clustering, the catastrophic evolution cluster has essentially been separated into three distinct sub-clusters, which we term *monarchic ejectors*, *intermediate ejectors*, and *cascading ejectors* (Figure 13).

The monarchic ejector systems are characterized by the highest ejection fractions of any cluster (0.659) but also the lowest median ejection velocity among the catastrophic groups ( $v_{\infty, \text{med}} = 2.293 \text{ km s}^{-1}$ ). The architectural parameters of these systems have distinct trends from the other clusters, allowing us to hypothesise the driving factors behind these differences. These systems begin with the highest average total masses ( $600 M_{\oplus}$ ) but the lowest median initial multiplicities (5 planets), and they lose an average of 2 planets over the course of the simulation, the lowest for any of the catastrophic sub-clusters. They also exhibit the highest initial gap complexity (0.13) and characteristic spacing (6.12) within the catastrophic sub-clusters. Importantly, they maintain relatively high mass partitioning (initial 0.19, final 0.18), a value closer to the quiet systems (0.18) than to other catastrophic sub-clusters. This suggests that a single massive planet retains gravitational dominance throughout the simulation. These properties suggest that the dynamical instability in the system is primarily driven by one body – the “monarch” – which dominates scattering and ejects a large fraction of the planetesimals. Ejections in this regime are therefore efficient but comparatively orderly, controlled by the gravitational influence of a single dominant planet. Minimal planetary orbital architectural changes occur, and the planetesimals are thus ejected in the same manner as they were by the quiet systems, but with a much more massive driver. This shows the continuum between our quiet ejector systems and the clusters which eject faster ISOs.

The cascading ejector systems display the most dramatic architectural evolution. They start with the highest multiplicities (6 planets) and lowest initial gap complexities (0.08) and characteristic spacings (5.87), reflecting tightly packed, quasi–“peas-in-a-pod” architectures. They have the lowest mass partitioning (0.07), meaning all the planets in these systems are similar in size. The cascading systems also start with the lowest mass of all of the catastrophic clusters ( $500 M_{\oplus}$ ), and lose the most mass throughout the simulation duration ( $108 M_{\oplus}$ ), the remnants of these systems being the lowest mass of all the systems, while still retaining the highest multiplicity (median 4, 84th percentile 5). The minimal changes to the mass partitioning indicate that the ejected planets are a similar mass to the remaining planets. The instabilities in these systems are thus hypothesised to take the pathway of chain reactions: once one planet is perturbed, tightly packed neighbours are destabilized, triggering further ejections and reordering. Planets cannot efficiently eject each other, but orbital perturbations can lead to planets and planetesimals kicked onto eccentric orbits. This creates path-crossing orbits that lead to frequent close encounters, and violent ejection events with high ejection velocities. The result is a “cascade” of dynamical interactions, with large-scale disruption of the planetary system and intense stirring of the planetesimal disc.

Overall, these sub-clusters illustrate that there are two pathways to ejecting many ISOs. Systems can either have a single massive planet which is able to drive slow ejections, or tightly-packed, less massive planets that can directly influence the planetesimal orbits when perturbing each other. The intermediate ejector systems occupy a middle ground, with ejection fractions of 0.597 and median ejection velocities around  $3.092 \text{ km s}^{-1}$  (between the monarchic and

cascading groups). They begin with initial masses, multiplicity, mass partitioning, gap complexity, and characteristic spacing also all intermediary. These systems fill in the continuum between the ejection mechanisms of the two types of catastrophic systems, and seem to consist of systems with less extreme versions of the system architectures in the other two clusters. Taken together, this points to instabilities driven by many intermediate-mass planets rather than a single dominant one. The resulting scattering has a smaller gravitational influence than the monarchic systems, so they cannot eject quite as many planetesimals, but do not have the similarly-sized planets which make the cascading ejectors so susceptible to chain events.

#### 4. DISCUSSION

##### 4.1. Dynamical Instability as an Interstellar Object Production Mechanism

Many dynamical instability triggers are thought to occur early in systems' lifetimes, when there are the most planetesimals available to eject. High-resolution simulations of the Solar System, initialized with realistic conditions, demonstrate that a very large fraction of planetesimals are eventually ejected, with N23 finding that  $\sim 93\%$  of the original small-body population is lost to interstellar space. We show here that 0.2-0.9 of the planetesimal disks we initiate are also ejected, becoming ISOs, in just the first 10 Myr of the evolution. If dynamical instability is as ubiquitous as has been suggested, then this process is indeed the dominant ISO production mechanism across the Galaxy.

Ejection velocity distributions evolve with system age. Planetesimals must first be scattered onto wide, high-perihelion orbits before the slowest velocity ejections can occur. The N23 simulations illustrate how the source regions of ISOs shift as a function of time, with distant ejections becoming increasingly common at later stages (see Figure 5). This temporal evolution may also influence the expected composition of ISOs: rocky bodies are preferentially ejected shortly after gas dispersal, while icy material is more likely to dominate the later, slower-ejection population. As shown in Figure 4 and in the velocity distribution snapshots of Figure 9, the fastest ISOs are typically produced early in a system's lifetime, whereas the slower, low-velocity tail emerges much later. In fact, the lowest-velocity ejections ( $v \lesssim 2 \times 10^{-2} \text{ km s}^{-1}$ ) in N23 only appear after  $\sim 20$  Myr of evolution.

The physical mechanisms responsible for these two regimes differ. Fast ejections generally result from a single strong scattering with a planet, occurring relatively close to the host star (see green points in Figure 3). In contrast, slow ejections are usually preceded by a gradual outward diffusion in semi-major axis before eventual unbinding, as seen in Figure 4. This highlights that dynamical instability produces a spectrum of outcomes: early, violent scattering yields fast ISOs, while orbital diffusion leads to the delayed production of slower-moving ISOs.

##### 4.2. Velocity Distributions as Tracers of System Architecture

To compare ISO velocity distributions across different dynamical ejection mechanisms, in Figure 14 we adapt a compilation figure from Pfalzner et al. (2021), incorporating literature to date and our Figure 13 cluster velocity medians. Ejection velocities vary significantly between ISO ejection mechanisms. Veras et al. (2014)'s white dwarf remnant scenario produces the slowest ISOs, with mean velocities of only  $\sim 0.065 \text{ km s}^{-1}$ , while stellar flybys yield moderately higher values ( $\sim 0.56 \text{ km s}^{-1}$ ). The subset of planet-planet scattering explored by Adams & Spiegel (2005), by contrast, appear to generate much faster<sup>2</sup> ISOs, with a median of  $5.4 \text{ km s}^{-1}$ . For comparison, N23's Solar System simulations report a median of  $0.96 \text{ km s}^{-1}$ . The low-velocity component in N23 aligns well with the peak of the white dwarf-remnant scenario. This may reflect the fact that late-time, low-energy ejections more closely resemble the stripping of a diffuse, loosely bound reservoir of material rather than the direct scattering of planetesimals by planets. Both the N23 and Veras et al. (2014) simulations included stellar flybys and Galactic tides, which could also contribute to the formation of this extended low-velocity tail.

Dynamical instabilities are distinctive producers of ISOs in that they span nearly the entire accessible ISO velocity space. This breadth arises from the variety of gravitational encounters possible, ranging from violent, close-in scatterings that launch material at high speed to more gradual, long-term orbital diffusion that produces slow, low-energy unbindings. Even within our relatively coarse, high-mass parameter space, we recover meaningful substructure in the velocity distributions. Given the enormous diversity of known exoplanet architectures, there is still commonality around instability-generated distributions relative to other production mechanisms. The ISO velocity distributions arising from planetary systems across the Galaxy are equally diverse.

If we could measure an ISO's ejection velocity, we could infer aspects of its birth system's architecture. This is a difficult task due to the influence of the Galaxy and its inhomogeneities (see section 4.3), but is within the realm of possibility for very young ISOs (ages  $\lesssim \text{Myr}$ ). These may be able to be traced, along with a large number of stars in the local volume observed by *Gaia*, back in time to identify the progenitor. The chances of this technique succeeding are very low (Forbes et al. 2025), especially for multi-Gyr-old ISOs like 3I/ATLAS (Hopkins et al. 2025b; Taylor & Seligman 2025). This has been attempted unsuccessfully for all three ISOs detected thus far within the Solar System (e.g. Pérez-Couto et al. 2025, for 3I). A more broadly viable route would be to use our results as an input in a Galactic-scale forward model for the distribution of ISO velocities.

##### 4.3. Connection to Observations and Galactic Population

<sup>2</sup> The large velocities reported in Adams & Spiegel (2005) may not be  $v_\infty$ , but rather a velocity when the ejected object is still close to the planet.

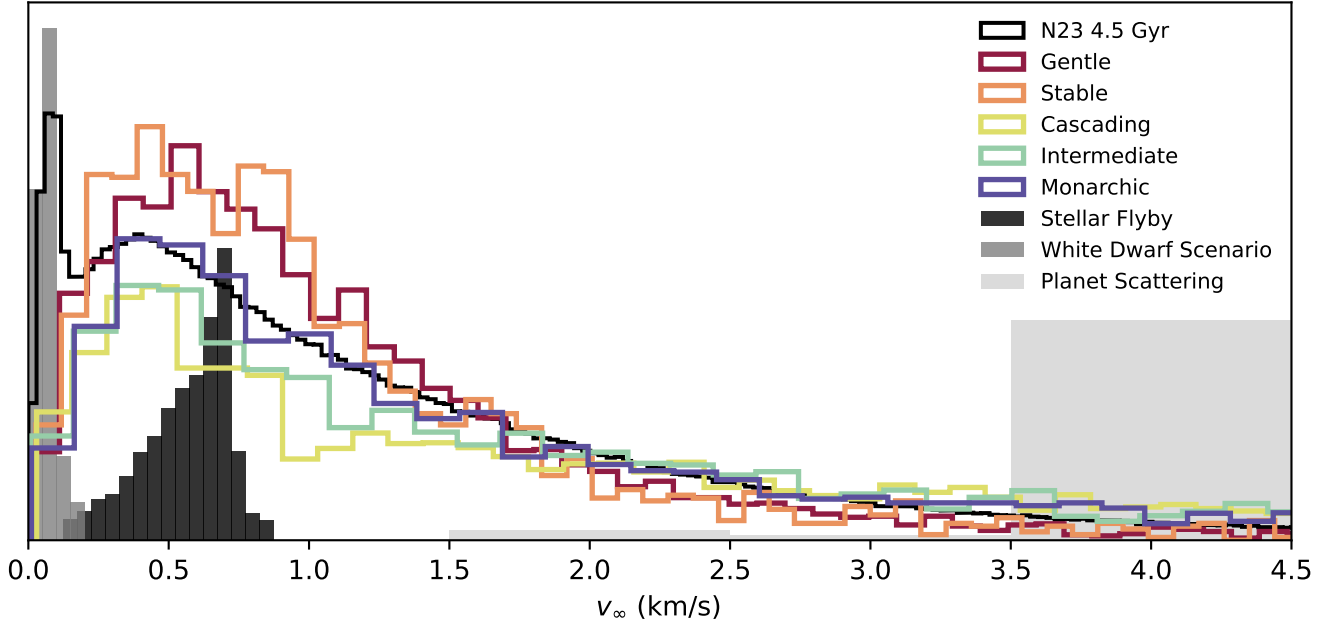


FIG. 14.— ISO ejection velocity distributions for various mechanisms. This is a modified version of the plot from Pfalzner et al. (2021), with an example of a velocity distribution from a stellar flyby from that paper, white dwarf scenario data from unpublished supplementary material of Veras et al. (2014), and planet–planet scattering data from Adams & Spiegel (2005). To these literature datasets, we add all ejections from the N23 simulation (black line), and representative example distributions from our simulation clusters (Figure 13). For each cluster, the simulation with the architecture parameters closest to the reported medians in Table 3 is displayed. Note that the Adams & Spiegel (2005) planet–planet scattering simulations had a higher velocity range, and most of the histogram has been truncated here. Data from both the planet–planet scattering simulations and the stellar flyby simulations are ambiguous as to whether the reported velocities are actually  $v_\infty$  or some other related velocity. Following Pfalzner et al. (2021), we assume they are  $v_\infty$  values for the purposes of this plot.

For a rare handful of locally passing ISOs, velocity is not the only diagnostic: observational campaigns can provide detailed constraints on their chemistry. Inbound measurements of the coma composition of the most recent interstellar comet 3I/ATLAS (e.g. Opitom et al. 2025; Puzia et al. 2025; Yang et al. 2025; Cordiner et al. 2025) have found a range of volatiles. Coma molecule production rates were also measured throughout perihelion passage for 2I/Borisov (e.g. Deam et al. 2025). Simulations suggest that future ISOs discovered by the Vera C. Rubin Observatory will also spend several hundred days at bright enough magnitudes to allow spectroscopy (Dorsey et al. 2025). While we do not explore chemistry here, understanding the compositional differences between ISOs released in the different ways illustrated in Figure 14 could allow for better linking of observed ISOs to the properties of their progenitor systems. Some work has been done by Hopkins et al. (2023) linking the metallicity gradient of the Galaxy to the ISO population, however using the composition of observed ISOs may provide more information about their release mechanism.

While close encounters with their planets can provide planetesimals with a larger kick, we have found that the typical ejection velocities of ISOs are much slower than the maximum limit. This is true even in systems where planets more massive than Jupiter are present, and in systems where the planets undergo a dynamical instability. This is because the typical interaction is much more modest, and the planetesimals execute a random walk in energy space until they are eventually unbound, as is expected even in single-planet scattering (e.g. Hadden & Tremaine 2024; Huang et al. 2025).

Comparatively slow ejection velocities have substantial downstream effects for how the planetesimals behave in the Galactic potential. When the planetesimals leave their home star system, they spread out into a long thin tidal stream due to the initial spread in velocities and the differential rotation implied by the Galaxy’s rotation curve. The typical length, width, and height of the streams are each proportional to the internal velocity dispersion of the stream (Dehnen & Hasanuddin 2018; Carlberg et al. 2024; Forbes et al. 2025), which in turn is initially set by the ejection velocity distribution. The streams will experience subsequent heating and perturbations in the Galactic potential, but will keep the imprint of the initial velocity distribution. The low velocities we find here imply that the streams will be denser, and therefore that fewer streams will contain the Sun (Forbes et al. 2025) at a given overall rate that ISOs encounter the Solar System. As a result, the rate of ISOs we will see in sky surveys may be supplied by a smaller number of streams, meaning that we are more likely to see multiple ISOs from the same stream star, and that the ISOs we see will be younger and more feasible to trace back to their parent star.

The velocity of the interstellar objects relative to their parent star is initially far smaller than the typical spread in velocities of the stellar population, which is about  $10\text{--}50\text{ km s}^{-1}$  depending on the component of motion and the age of the stars under consideration (e.g. Holmberg et al. 2009; Gaia Collaboration et al. 2018). This validates the frequent earlier assumption that the ISO population may be traced by the population of stars. Note that this still requires appropriate reweighting of stars to account for trends in the ISO production rate as a function of other stellar



properties, most notably metallicity (Hopkins et al. 2025a). Eventually the ISOs will also be subject to dynamical heating due to perturbers in the Galactic potential (e.g. Spitzer & Schwarzschild 1951; Lacey 1984; Forbes et al. 2012) on timescales  $\gtrsim 100$  Myr. This increases the spread in velocities of ISOs at a given location. Meanwhile, even without heating, the velocity of an ISO will typically be substantially different from its particular host star because they are on different orbits and therefore drift apart in the Galaxy. A given stream of ISOs will have a length of order its velocity dispersion times its age (Forbes et al. 2025). Nonetheless, because the stars are subject to the same dynamical heating and orbit in the same potential, once any biases<sup>3</sup> in ISO production as a function of stellar properties have been accounted for, the only remaining difference originates from the ejection velocities. Because the ejection velocities are small (Figure 14) compared to the typical spread in stellar velocities, it is the dynamics of the Galaxy and not the ejections, that determine the distribution of velocities of the ISOs we will observe in the Solar System. Stream-related effects, namely the possibility of finding multiple ISOs from the same star, are much more sensitive to the ejection velocity distribution (Forbes et al. 2025).

#### 4.4. Re-scaleability for wider use

Our simulations are described as planetary systems orbiting a Solar-mass, with orbital distances expressed in au and masses in Solar masses. However, because gravity is scale-free and our simulations omit scale-dependent effects such as the Galactic tide, the results can be rescaled, to represent systems of different stellar masses or orbital scales. If we scale the mass by a factor  $x$ , so that the new masses in the system are  $\tilde{M} = xM$ , and similarly scale the distances by a factor  $y$ , then the ejection fractions and all of the system architecture parameters, besides Total Mass, will be unchanged, but the ejection velocities will be affected. In particular, all velocities in the simulation, including ejection velocities, will be scaled as

$$\tilde{v} = v \sqrt{\frac{x}{y}}. \quad (5)$$

Thus, more extended or lower-mass systems will eject material more slowly, while higher-mass or more compact systems will produce faster ejecta in physical units ( $\text{km s}^{-1}$ ).

It is important to note that we do not have complete freedom to set the ejection velocities to arbitrary values by carrying out this rescaling. Stellar and disc properties impose correlations between  $x$  and  $y$ . For example, lower-mass stars are generally associated with smaller protoplanetary discs (e.g. Andrews 2020), which naturally lead to more compact planetary systems. This coupling implies that realistic rescaling will shift the velocity distributions only modestly, rather than producing drastic changes.

### 5. CONCLUSION

In this work, we have investigated how dynamical instabilities influence the ejection of interstellar objects (ISOs) from planetary systems with massive planets and planetesimal discs. By simulating 2,461 systems for 10 Myr, and exploring a wide range of total system masses (300-800  $M_{\oplus}$ ), multiplicities (3-7 planets), and initial orbital configurations, we characterise the velocity and inclination distributions of ejected material as a function of system architecture.

We find that we can split our systems into two distinct evolutionary pathways. *Quiet evolution* systems have low initial multiplicities (median 4) and wide orbital spacing (median 8.2 mutual Hill radii). These systems remain stable, ejecting a median of 28.4% of their planetesimals with a median velocity of  $1.611 \text{ km s}^{-1}$ . In contrast, the *catastrophic evolution* systems have high initial multiplicities (median 6), and more compact orbital architectures (median 5.9 mutual Hill radii). The systems in this cluster eject a median 59% of their planetesimals, at higher velocities ( $2.9 \text{ km s}^{-1}$ ). The two populations undergo different evolutionary pathways, with the catastrophic systems ejecting a median  $89.4 M_{\oplus}$  of planetary mass, and increasing orbital separations by eight mutual Hill radii. The *quiet* systems have minimal orbital changes, retaining their planetary architectures.

Within each population, we further divided the clusters to understand the mechanisms separating the populations. Catastrophic systems split into three classes: *monarchic ejectors*, where a single massive planet dominates scattering, producing large ejection fractions (66%) at low velocities; *cascading ejectors*, where similarly-sized planets in tightly-packed configurations trigger violent instabilities, with many orbital crossings and high energy ejections; and finally, an *intermediate ejector* subcluster which falls in the middle group between these extremes. The quiet systems were split into *stable systems*, which undergo minimal orbital evolution, and *gentle ejectors*, which produce moderate ISO populations through orbital diffusion, similar to the monarchic ejectors but without enough mass for efficient scattering. These classifications demonstrate that initial system architectures — most significantly multiplicity, mass partitioning, total mass, and orbital spacing — determine the efficiency and kinematics of a system’s ISO ejections.

We compared our results with a longer-running Solar System simulation from N23 to show that our results capture the early, instability-driven phase of ISO production. Our velocity distributions at 10 Myr were similar to the Solar System simulation at the same epoch. The Solar System ISO velocity distribution develops a low-velocity tail between 1-100 Myrs, driven by the Galactic tide and stellar flybys.

Our results have several implications for the Galactic ISO population. The relatively slow ejection velocities we find here indicate that ISOs will initially orbit in the Galaxy in dense, narrow tidal streams with small internal velocity distributions, until they are heated by inhomogeneities in the Galactic potential. All else equal, this fact increases

<sup>3</sup> Admittedly these biases are not known, but trends with the occurrence of planets as a function of host star properties may provide guidance (see Zhu & Dong 2021, for a review).

the likelihood of detecting multiple ISOs from the same progenitor system. At the same time, the comparatively low ejection velocities we find here provides more evidence for the common assumption that the velocity distribution function of ISOs that the Solar System encounters will be set mostly by the distribution function of the stars.

While our simulations omit several effects — Galactic tides, collisions and planetary radii effects, and self-stirring of the planetesimal disc — they isolate the fundamental gravitational dynamics between the planets, and demonstrate how system architectures impact ISO production efficiency and velocity distributions. The scale-free nature of gravity also allows our results to be rescaled to systems of other masses or orbital radii. Future work incorporating longer integration times, more physically-motivated planetary architectures, and simulations placed in their Galactic context, will help to refine predictions and assess how robust they are across a broader swath of the planetary system parameter space.

If dynamical instabilities are a common process, this would be the main release mechanism for the Galactic ISO population. The properties of ejected ISOs retain a measurable imprint of their parent system’s architecture and age — creating the possibility, through challenging, of using ISOs as a form of Galactic archaeology. As our observed sample of ISOs grows (e.g. through the Vera C. Rubin Observatory’s LSST, predicted to find  $\sim 1$  ISO per year by Dorsey et al. (2025)), the detected population will provide tests to the mechanisms and galactic propagation we predict. Understanding this link is key to interpreting the growing observational catalogue of interstellar interlopers and reconstructing the dynamical histories of planetary systems throughout the Galaxy.

#### ACKNOWLEDGMENTS

M.T.B. and J.C.F. appreciate support by the Rutherford Discovery Fellowships from New Zealand Government funding, administered by the Royal Society Te Apārangi. We are grateful to Chris Lintott for thoughtful feedback on the manuscript, and to Susanne Pfalzner, Simon Portegies Zwart, Matthew Hopkins, W. Garrett Levine, Joe Masiero, and Matthew Holman for helpful conversations.

Simulations were carried out using *rebound* (Rein & Liu 2012; Rein & Tamayo 2015; Rein et al. 2019; Rein & Tamayo 2017). Data analysis was performed using *NumPy* (Harris et al. 2020), *pandas* (Wes McKinney 2010; pandas development team 2025) *Astropy* (Astropy Collaboration et al. 2013, 2018, 2022), *scikit-learn* (Pedregosa et al. 2011), *dynesty* (Koposov et al. 2024), *SciPy* (Virtanen et al. 2020). Graphs were produced using *Matplotlib* (Hunter 2007).

#### APPENDIX

The box and whisker plots for the data presented in Table 2 and Table 3 are presented in Figure 15 and Figure 16 respectively. These are the distributions of the system architecture parameters within each of the clusters found in the  $k = 2$  and  $k = 5$   $k$ -means clustering analyses.

#### REFERENCES

- Adams, F. C., & Spiegel, D. N. 2005, *Astrobiology*, 5, 497, doi: [10.1089/ast.2005.5.497](https://doi.org/10.1089/ast.2005.5.497)
- Alexander, R., Pascucci, I., Andrews, S., Armitage, P., & Cieza, L. 2014, *Protostars and Planets VI*, Henrik Beuther, Ralf S. Klessen, Cornelis P. Dullemond, and Thomas Henning (eds.), University of Arizona Press, Tucson, p.475-496, 475, doi: [10.2458/azu\\_uapress\\_9780816531240-ch021](https://doi.org/10.2458/azu_uapress_9780816531240-ch021)
- Andrews, S. M. 2020, *Annual Review of Astronomy and Astrophysics*, 58, 483, doi: [10.1146/annurev-astro-031220-010302](https://doi.org/10.1146/annurev-astro-031220-010302)
- Astropy Collaboration, Robitaille, T. P., Tollerud, E. J., et al. 2013, *A&A*, 558, A33, doi: [10.1051/0004-6361/201322068](https://doi.org/10.1051/0004-6361/201322068)
- Astropy Collaboration, Price-Whelan, A. M., Sipőcz, B. M., et al. 2018, *AJ*, 156, 123, doi: [10.3847/1538-3881/aabc4f](https://doi.org/10.3847/1538-3881/aabc4f)
- Astropy Collaboration, Price-Whelan, A. M., Lim, P. L., et al. 2022, *ApJ*, 935, 167, doi: [10.3847/1538-4357/ac7c74](https://doi.org/10.3847/1538-4357/ac7c74)
- Bannister, M. T., Gladman, B. J., Kavelaars, J. J., et al. 2018, *The Astrophysical Journal Supplement Series*, 236, 18, doi: [10.3847/1538-4365/aab77a](https://doi.org/10.3847/1538-4365/aab77a)
- Carlberg, R. G., Jenkins, A., Frenk, C. S., & Cooper, A. P. 2024, *ApJ*, 975, 135, doi: [10.3847/1538-4357/ad7b35](https://doi.org/10.3847/1538-4357/ad7b35)
- Cordiner, M. A., Roth, N. X., Kelley, M. S. P., et al. 2025, *ApJ*, 991, L43, doi: [10.3847/2041-8213/ae0647](https://doi.org/10.3847/2041-8213/ae0647)
- Dawson, R. I., & Johnson, J. A. 2018, *Annual Review of Astronomy and Astrophysics*, 56, 175, doi: [10.1146/annurev-astro-081817-051853](https://doi.org/10.1146/annurev-astro-081817-051853)
- Deam, S. E., Bannister, M. T., Opatom, C., et al. 2025, *arXiv e-prints*, arXiv:2507.05051, doi: [10.48550/arXiv.2507.05051](https://doi.org/10.48550/arXiv.2507.05051)
- Dehnen, W., & Hasanuddin. 2018, *MNRAS*, 479, 4720, doi: [10.1093/mnras/sty1726](https://doi.org/10.1093/mnras/sty1726)
- Dorsey, R. C., Hopkins, M. J., Bannister, M. T., et al. 2025, *Planetary Science Journal*, 6, 214, doi: [10.3847/PSJ/adf8ca](https://doi.org/10.3847/PSJ/adf8ca)
- Drażkowska, J., Bitsch, B., Lambrechts, M., et al. 2023, in *Astronomical Society of the Pacific Conference Series*, Vol. 534, *Protostars and Planets VII*, ed. S. Inutsuka, Y. Aikawa, T. Muto, K. Tomida, & M. Tamura, 717, doi: [10.48550/arXiv.2203.09759](https://doi.org/10.48550/arXiv.2203.09759)
- Eriksson, L. E. J., Ronnet, T., & Johansen, A. 2021, *Astronomy & Astrophysics*, 648, A112, doi: [10.1051/0004-6361/202039889](https://doi.org/10.1051/0004-6361/202039889)
- Fernández, J. A. 1997, *Icarus*, 129, 106, doi: [10.1006/icar.1997.5754](https://doi.org/10.1006/icar.1997.5754)
- Forbes, J., Krumholz, M., & Burkert, A. 2012, *ApJ*, 754, 48, doi: [10.1088/0004-637X/754/1/48](https://doi.org/10.1088/0004-637X/754/1/48)
- Forbes, J. C., Bannister, M. T., Lintott, C., et al. 2025, *ApJ*, 988, 121, doi: [10.3847/1538-4357/adc9ac](https://doi.org/10.3847/1538-4357/adc9ac)
- Gaia Collaboration, Katz, D., Antoja, T., et al. 2018, *A&A*, 616, A11, doi: [10.1051/0004-6361/201832865](https://doi.org/10.1051/0004-6361/201832865)
- Gautham Bhaskar, H., & Perets, H. 2025, *arXiv e-prints*, arXiv:2501.13166, doi: [10.48550/arXiv.2501.13166](https://doi.org/10.48550/arXiv.2501.13166)
- Gilbert, G. J., & Fabrycky, D. C. 2020, *The Astronomical Journal*, 159, 281, doi: [10.3847/1538-3881/AB8E3C](https://doi.org/10.3847/1538-3881/AB8E3C)
- Hadden, S., & Tremaine, S. 2024, *MNRAS*, 527, 3054, doi: [10.1093/mnras/stad3478](https://doi.org/10.1093/mnras/stad3478)
- Harris, C. R., Millman, K. J., van der Walt, S. J., et al. 2020, *Nature*, 585, 357, doi: [10.1038/s41586-020-2649-2](https://doi.org/10.1038/s41586-020-2649-2)
- Hasegawa, Y., Haworth, T. J., Hoadley, K., et al. 2022, *The Astrophysical Journal Letters*, 926, L23, doi: [10.3847/2041-8213/ac50aa](https://doi.org/10.3847/2041-8213/ac50aa)
- Holmberg, J., Nordström, B., & Andersen, J. 2009, *A&A*, 501, 941, doi: [10.1051/0004-6361/200811191](https://doi.org/10.1051/0004-6361/200811191)
- Hopkins, M. J., Bannister, M. T., & Lintott, C. 2025a, *AJ*, 169, 78, doi: [10.3847/1538-3881/ad9eb3](https://doi.org/10.3847/1538-3881/ad9eb3)
- Hopkins, M. J., Dorsey, R. C., Forbes, J. C., et al. 2025b, *ApJ*, 990, L30, doi: [10.3847/2041-8213/adfbf4](https://doi.org/10.3847/2041-8213/adfbf4)

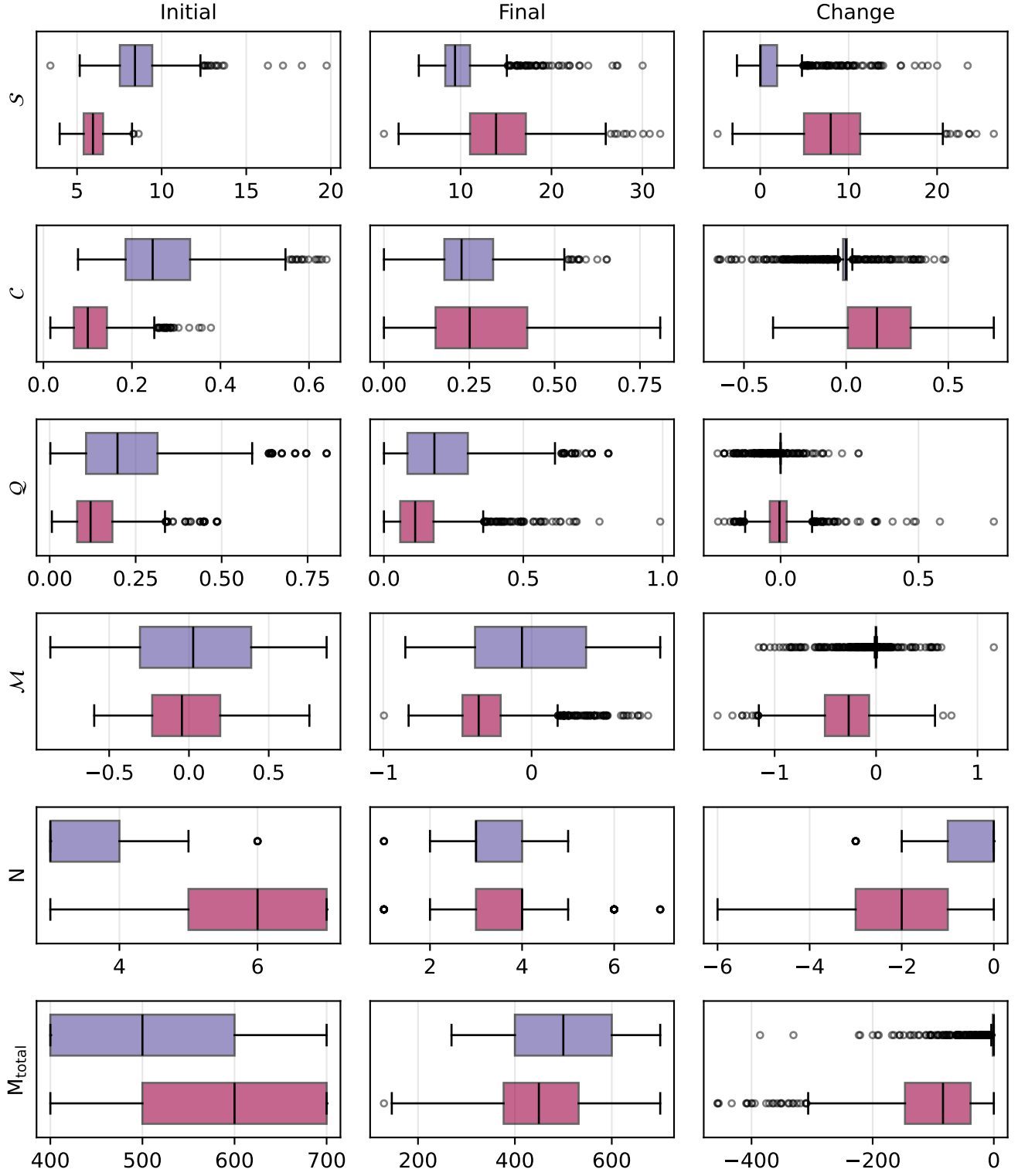


FIG. 15.— Box plots showing the spread of the system architecture parameters for the each broad cluster. Parameter distributions for *catastrophic evolution* systems are shown in red, and the *quiet evolution* systems are shown in blue.

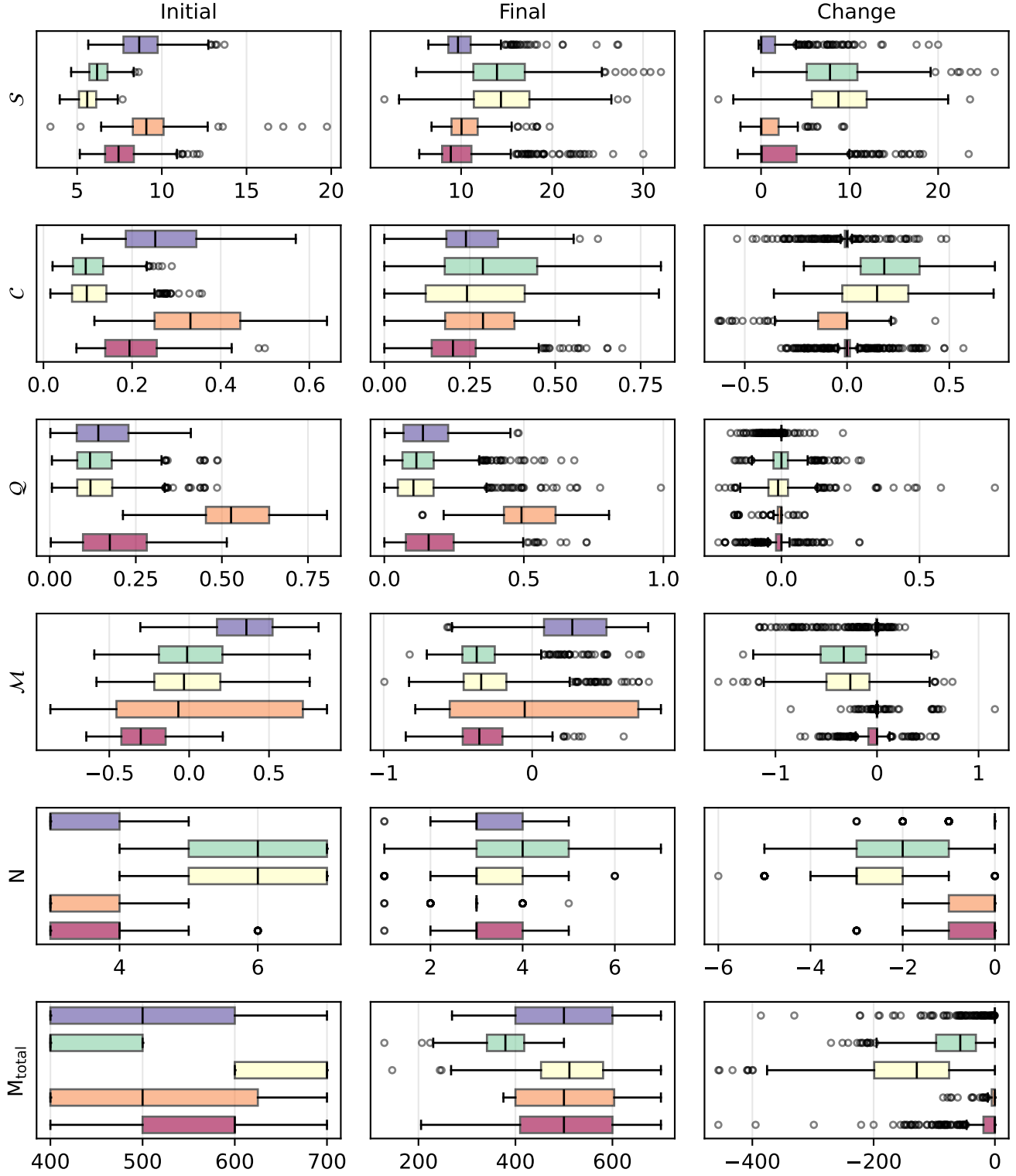


FIG. 16.— Box plots showing the spread of system architecture parameters for the subclusters. The plots match the colours in Figure 13, with gentle (red) and stable (orange) the subclusters for the *quiet evolution* cluster, and monarchic (blue), intermediate (green) and cascading (yellow) the subclusters for the *catastrophic evolution* cluster.



- Hopkins, M. J., Lintott, C., Bannister, M. T., Mackereth, J. T., & Forbes, J. C. 2023, *The Astronomical Journal*, 166, 241, doi: [10.3847/1538-3881/ad03e6](https://doi.org/10.3847/1538-3881/ad03e6)
- Huang, Y., Gladman, B., & Kokubo, E. 2025, arXiv e-prints, arXiv:2511.16056, doi: [10.48550/arXiv.2511.16056](https://doi.org/10.48550/arXiv.2511.16056)
- Hunter, J. D. 2007, *Computing in Science & Engineering*, 9, 90, doi: [10.1109/MCSE.2007.55](https://doi.org/10.1109/MCSE.2007.55)
- Izidoro, A., Ogihara, M., Raymond, S. N., et al. 2017, *Monthly Notices of the Royal Astronomical Society*, 470, 1750, doi: [10.1093/mnras/stx1232](https://doi.org/10.1093/mnras/stx1232)
- Koposov, S., Speagle, J., Barbary, K., et al. 2024, *dynesty: v2.1.4*, Zenodo, doi: [10.5281/zenodo.12537467](https://doi.org/10.5281/zenodo.12537467)
- Lacey, C. G. 1984, *MNRAS*, 208, 687, doi: [10.1093/mnras/208.4.687](https://doi.org/10.1093/mnras/208.4.687)
- Laughlin, G., & Batygin, K. 2017, *Research Notes of the AAS*, 1, 43, doi: [10.3847/2515-5172/aaa02b](https://doi.org/10.3847/2515-5172/aaa02b)
- Levine, W. G., Taylor, A. G., Seligman, D. Z., et al. 2023, *Planetary Science Journal*, 4, doi: [10.3847/PSJ/acdf58](https://doi.org/10.3847/PSJ/acdf58)
- Levison, H. F., Morbidelli, A., Nacional, O., De Janeiro, R., & Backman, D. 2007, in *Protostars and Planets V* (University of Arizona Press), 669–684
- Lintott, C., Bannister, M. T., & Mackereth, J. T. 2021, *The Astrophysical Journal Letters*, 924, L1, doi: [10.3847/2041-8213/ac41d5](https://doi.org/10.3847/2041-8213/ac41d5)
- Liu, B., Raymond, S. N., & Jacobson, S. A. 2022, *Nature*, 604, 643, doi: [10.1038/s41586-022-04535-1](https://doi.org/10.1038/s41586-022-04535-1)
- Lovis, C., & Fischer, D. 2010, in *Exoplanets*, ed. S. Seager (Tucson: University of Arizona Press), 27–53. <https://ui.adsabs.harvard.edu/abs/2010exop.book...27L>
- Malmberg, D., Davies, M. B., & Heggie, D. C. 2011, *Monthly Notices of the Royal Astronomical Society*, 411, 859, doi: [10.1111/j.1365-2966.2010.17730.x](https://doi.org/10.1111/j.1365-2966.2010.17730.x)
- Morbidelli, A. 2018, in *Handbook of Exoplanets*, ed. H. Deeg & J. Belmonte (Springer International Publishing), 2523–2541, doi: [10.1007/978-3-319-55333-7\\_145](https://doi.org/10.1007/978-3-319-55333-7_145)
- Moro-Martín, A., Turner, E. L., & Loebe, A. 2009, *The Astrophysical Journal*, 704, 733, doi: [10.1088/0004-637X/704/1/733](https://doi.org/10.1088/0004-637X/704/1/733)
- Müller, S., Baron, J., Helled, R., Bouchy, F., & Parc, L. 2024, *A&A*, 686, A296, doi: [10.1051/0004-6361/202348690](https://doi.org/10.1051/0004-6361/202348690)
- Nesvorný, D., Bernardinelli, P., Vokrouhlický, D., & Batygin, K. 2023, *Icarus*, 406, 115738, doi: [10.1016/j.icarus.2023.115738](https://doi.org/10.1016/j.icarus.2023.115738)
- Opitom, C., Snodgrass, C., Jehin, E., et al. 2025, *MNRAS*, 544, L31, doi: [10.1093/mnrasl/slaf095](https://doi.org/10.1093/mnrasl/slaf095)
- pandas development team, T. 2025, *pandas-dev/pandas: Pandas, v2.3.1*, Zenodo, doi: [10.5281/zenodo.15831829](https://doi.org/10.5281/zenodo.15831829)
- Pedregosa, F., Varoquaux, G., Gramfort, A., et al. 2011, *Journal of Machine Learning Research*, 12, 2825
- Pérez-Couto, X., Torres, S., Villaver, E., Mustill, A. J., & Manteiga, M. 2025, arXiv e-prints, arXiv:2509.07678, doi: [10.48550/arXiv.2509.07678](https://doi.org/10.48550/arXiv.2509.07678)
- Pfalzner, S., Aizpuru Vargas, L. L., Bhandare, A., & Veras, D. 2021, *Astronomy & Astrophysics*, 651, A38, doi: [10.1051/0004-6361/202140587](https://doi.org/10.1051/0004-6361/202140587)
- Pfalzner, S., Govind, A., & Portegies Zwart, S. 2024, *Nature Astronomy*, 8, 1380, doi: [10.1038/s41550-024-02349-x](https://doi.org/10.1038/s41550-024-02349-x)
- Puzia, T. H., Rahatgaonkar, R., Carvajal, J. P., Nayak, P. K., & Lucio, B. 2025, *Spectral Characteristics of Interstellar Object 3I/ATLAS from SOAR Observations*, arXiv, doi: [10.48550/arXiv.2508.02777](https://doi.org/10.48550/arXiv.2508.02777)
- Raymond, S. N., Kaib, N. A., Armitage, P. J., & Fortney, J. J. 2020, *The Astrophysical Journal Letters*, doi: [10.3847/2041-8213/abc55f](https://doi.org/10.3847/2041-8213/abc55f)
- Rein, H., & Liu, S.-F. 2012, *Astronomy & Astrophysics*, 537, A128, doi: [10.1051/0004-6361/201118085](https://doi.org/10.1051/0004-6361/201118085)
- Rein, H., & Tamayo, D. 2015, *Monthly Notices of the Royal Astronomical Society*, 452, 376, doi: [10.1093/mnras/stv1257](https://doi.org/10.1093/mnras/stv1257)
- Rein, H., & Tamayo, D. 2017, *MNRAS*, 467, 2377, doi: [10.1093/mnras/stx232](https://doi.org/10.1093/mnras/stx232)
- Rein, H., Hernandez, D. M., Tamayo, D., et al. 2019, *Monthly Notices of the Royal Astronomical Society*, 485, 5490, doi: [10.1093/mnras/stz769](https://doi.org/10.1093/mnras/stz769)
- Safronov, V. S. 1972, in *The Motion, Evolution of Orbits, and Origin of Comets*, Vol. 45, Leningrad, U.S.S.R.
- Spitzer, Jr., L., & Schwarzschild, M. 1951, *ApJ*, 114, 385, doi: [10.1086/145478](https://doi.org/10.1086/145478)
- Stern, S. A. 1990, *Publications of the Astronomical Society of the Pacific*, 102, 793, doi: [10.1086/132704](https://doi.org/10.1086/132704)
- Taylor, A. G., & Seligman, D. Z. 2025, *ApJ*, 990, L14, doi: [10.3847/2041-8213/adfa28](https://doi.org/10.3847/2041-8213/adfa28)
- The ‘Oumuamua ISSI Team, Bannister, M. T., Bhandare, A., et al. 2019, *Nature Astronomy*, 3, 594, doi: [10.1038/s41550-019-0816-x](https://doi.org/10.1038/s41550-019-0816-x)
- Veras, D., Shannon, A., & Gänsicke, B. T. 2014, *Monthly Notices of the Royal Astronomical Society*, 445, 4175, doi: [10.1093/mnras/stu2026](https://doi.org/10.1093/mnras/stu2026)
- Virtanen, P., Gommers, R., Oliphant, T. E., et al. 2020, *Nature Methods*, 17, 261, doi: [10.1038/s41592-019-0686-2](https://doi.org/10.1038/s41592-019-0686-2)
- Wes McKinney. 2010, in *Proceedings of the 9th Python in Science Conference*, ed. Stéfan van der Walt & Jarrod Millman, 56 – 61, doi: [10.25080/Majora-92bf1922-00a](https://doi.org/10.25080/Majora-92bf1922-00a)
- Wisdom, J., & Holman, M. 1991, *The Astronomical Journal*, 102, 1528, doi: [10.1086/115978](https://doi.org/10.1086/115978)
- Wyatt, M. C., Bonsor, A., Jackson, A. P., Marino, S., & Shannon, A. 2017, *Monthly Notices of the Royal Astronomical Society*, 464, 3385, doi: [10.1093/mnras/stw2633](https://doi.org/10.1093/mnras/stw2633)
- Yang, B., Meech, K. J., Connolly, M., & Keane, J. V. 2025, *Spectroscopic Characterization of Interstellar Object 3I/ATLAS: Water Ice in the Coma*, arXiv, doi: [10.48550/arXiv.2507.14916](https://doi.org/10.48550/arXiv.2507.14916)
- Zhu, W., & Dong, S. 2021, *ARA&A*, 59, 291, doi: [10.1146/annurev-astro-112420-020055](https://doi.org/10.1146/annurev-astro-112420-020055)